MAREES TERRESTRES

BULLETIN D'INFORMATIONS

INTERNATIONAL CENTER FOR EARTH TIDES
CENTRE INTERNATIONAL DES MAREES TERRESTRES

Federation of Astronomical and Geophysical Data Analysis Services (FAGS)

International Association of Geodesy - International Gravity Field Service (IAG – IGFS)

Publié avec le soutien de l'Observatoire Royal de Belgique

BIM
1 4 3

15 DECEMBRE 2007

Editeur: Dr. Bernard DUCARME
Observatoire Royal de Belgique
Avenue Circulaire 3
B-1180 Bruxelles

BIM 143

15 décembre 2007

Jena meeting (end)

Additional papers

Influence of the equilibrium ocean pole tide on the gravity field

CHEN Xiaodong[1, 2], DUCARME Bernard[3], SUN Heping[1]

1) Key Laboratory of Dynamical Geodesy, Institute of Geodesy and Geophysics, Chinese Academy of Sciences, Xudong Street 340, Wuhan, China, 430077;

2) Graduate School of Chinese Academy of Sciences, Yuquan Road 19A, Beijing, China, 100049

3) Research Associate NFSR, Royal Observatory of Belgium, Av. Circulaire 3, B-1180, Brussels, Belgium

Summary : Although there is a lot of investigations on the ocean pole tide, there are not so many publications of its contribution to the gravity field. One of the reasons may be that both the ocean pole tide and the gravity pole tide are not easily determined by observations, as they are weak and, being close to the annual period, disturbed seriously by other geophysical phenomena, such as atmospheric and oceanic global circulation. With the development of the observation techniques, these two kinds of signals can be determined now. Results from the TOPEX/Poseidon (T/P) satellite altimetry for detecting the ocean pole tide confirm that the long-wavelength component of the geocentric pole tide deformations due to the Chandler wobble is consistent with the self-consistent equilibrium response model and the classical equilibrium one can only explain 70% of the variations. In addition, the superconduting gravimeters (SG) are now able to record and determine the gravity effect caused by polar motion. It is due to their high precision (as high as 10^{-11} m.s^{-2}) and very low drift (only at the level of 10 nm.s^{-2} per year). Thus it is meaningful to estimate the contribution of the ocean pole tide to the gravity field now.

On the assumption that the ocean pole tide is in equilibrium, the loading gravity effects of both the classical and the self-consistent ocean pole tide are calculated at each of the 9 SG stations where gravity pole tide has been determined by Ducarme & al. [2006]. Then, after introducing a well-chosen phase lag, the amplitude of the ocean pole tide gravimetric vector at each of these stations is estimated with a linear fit method. Numerical results demonstrate that the amplitude of the loading gravity effect of the ocean pole tide is at the level of 10^{-9} ms^{-2} and that its phase lag is not negligible. The contribution of the self-consistent ocean pole tide to the gravity field variations cannot be ignored as it can increases the amplitude of the pole tide gravimetric factor by more than two per cent, but its effect on the phase remains negligible. The self-consistent model predicts effects 10% larger than the classical one.

1. Introduction

Both the ocean pole tide and the gravity pole tide are weak signals disturbed by many geophysical factors. Therefore, they are difficult to determine. The ocean pole tide is the ocean response to the variation of the centrifugal force. The equilibrium ocean pole tide assumes that the displaced ocean surface is in equilibrium with the equipotential surface [Lambeck 1988; Munk and Macdonald, 1960]. The classical equilibrium ocean pole tide is an equilibrium ocean pole tide conserving mass in non-global oceans overlying an elastic earth [Haubrich and Munk 1959; Dickman 1985; Desai 2002]. The self-consistent ocean pole tide further includes the tidal loading and the self-gravitation, in addition to the classical equilibrium ocean pole tide [Dahlen 1976; Agnew 1978; Desai 2002]. The assumption of an equilibrium ocean pole tide is controversial in the investigation of the ocean pole tide [Proudman 1960; Munk and Macdonald, 1960; Wunsch 1974; Naito, 1979, 1983; O'Connor 1983; Dickman 1985]. Recent results from TOPEX/Poseidon (T/P) satellite altimetry demonstrate that the long-wavelength

component of the geocentric pole tide deformations at the Chandler period is consistent with the theoretical self-consistent equilibrium response and can explain 70% of variations of the theoretical classical equilibrium response [Desai, 2002]. In addition, the superconduting gravimeters (SG) are able to record and precisely determine the gravity effect caused by polar motion, thanks to their high precision (as high as 10^{-11} ms^{-2}) and very low drift (only at the level of 10 nms^{-2} per year). Thus the deployment of SG's in the framework of the Global Geodynamics Project (GGP) provides an opportunity to determine accurately the pole tide gravity effect [Crossely 1999; Loyer 1999; Xu J. Q. 2004; Harnisch 2006; Ducarme et al., 2006]. Consequently, we have the reason and the possibility to estimate the influence of ocean pole tide on gravity field now.

There are only a few publications on the tidal loading effect of the ocean pole tide. Assuming that the pole tide is in equilibrium and has no phase lag, Hinderer and Legros point out that the pole tide gravimetric factor increases by 0.04, in the case of global oceans without continent [Hinderer and Legros 1989]. If the non-global oceans are used, a rough computation taking into account the degree 0 order 0 of the ocean function is done by Dehant, the increase is 0.025. And the phase shifts rang from 9º to 22º with an uncertainty of about 5º [Dehant and Zschau 1989]. Loyer introduces the work of Hinderer and Dehant when he tries to explain the influence of ocean pole tide on gravity field [Loyer 1999]. And Boy shows that the amplitude of the gravimeter factor increases from the theoretical value for an elastic Earth 1.16 to 1.185 and the phase lag is less than 0.5º after taking into account a static model of oceanic pole tide [Boy, 2000]. Xu J.Q. substitutes loading vector of Chandler period with that of the long period tidal wave S_{Sa} to estimate the influence of the ocean pole tide on the pole tide gravimetric factor, and the increase is about 0.024 [Xu J. Q. 2004]. The emphasis of all these previous works is not to estimate the influence of the ocean pole tide so that only brief introductions are given in these works.

In this paper, we give a detailed description of the influence of the equilibrium ocean pole tide on the gravity field. The theoretical gravity pole tide is computed in advance. Then the gravity loading effect of the classical and the self-consistent ocean pole tide are computed, respectively. After manually introducing a proper phase lag in the calculation of the gravity loading effect, the relative amplitude of the loading pole tide with respect to the theoretical gravity pole tide is obtained by fitting the gravity loading effect and the theoretical gravity pole tide with a linear fit method. We present here the relative gravity loading vectors (amplitude factor and phase lag) of all the GGP stations. But only station Brussels is discussed in the paper because the processing is similar to all the other stations.

2. The pole tide potential

In an Earth's fixed rotating coordinate system with its mean rotation axis is initially aligned with the z axis of the coordinate system, x is oriented along the Greenwich meridian, and y along the 90ºE meridian, the instantaneous rotation vector $\vec{\omega}(t)$ can be expressed as

$$\vec{\omega}(t) = \Omega\left[m_1(t) \quad m_2(t) \quad \left(1 + m_3(t)\right)\right] \tag{1}$$

where Ω is the mean rotation rate of the Earth, Ω = 7.292115×10^{-5} rad·s^{-1}; $m_1(t)$ and $m_2(t)$ describe the polar motion, $m_3(t)$ describes the Earth's rotation rate. The small time depending variables $m_i(t)$ are usually defined in terms of small quantities ($m_i(t) << 1$) [Lambeck, 1988; Munk and Macdonald, 1960]. To the first order $m_1(t)$ and $m_2(t)$ are the angular offsets of the instantaneous rotation vector from the z axis of the defined coordinate system, in the direction of the x axis and y axis of the coordinate system, respectively.

The instantaneous centrifugal potential $V_c(x, y, z)$ at an arbitrary point on the Earth $\vec{r} = (x, y, z)$, can be written to the first order in $m_i(t)$, as [Wahr 1985].

$$\begin{aligned} V_c(x, y, z) &= \frac{1}{2}\left[|\vec{\omega}(t)|^2 |\vec{r}|^2 - (\vec{\omega}(t) \cdot \vec{r})^2\right] \\ &= \frac{\Omega^2}{2}\left[(1 + 2m_3(t))(x^2 + y^2) - 2z(xm_1(t) + ym_2(t))\right] \end{aligned} \tag{2}$$

The time dependant differential centrifugal potential $V(x, y, z, t)$ is then obtained by subtracting the centrifugal potential $\overline{V}_c(x, y, z)$ induced by the initial mean rotation vector $\vec{\omega}_0$ from the instantaneous centrifugal potential $V_c(x, y, z)$.

$$\begin{aligned} &V(x, y, z, t) = V_c(x, y, z) - \overline{V}_c(x, y, z) = \frac{\Omega^2}{2}\left[2m_3(t)(x^2 + y^2) - 2z(xm_1(t) + ym_2(t))\right] \\ &\vec{\omega}_0 = [0 \quad 0 \quad \Omega] \quad , \quad \overline{V}_c(x, y, z) = \frac{\Omega^2}{2}\left[x^2 + y^2\right] \end{aligned} \tag{3}$$

The magnitude of the variations in the rotation rate $m_3(t)$ is at least two orders smaller than that of variations in the pole coordinates $m_1(t)$ and $m_2(t)$. Therefore, the contribution of $m_3(t)$ to the differential centrifugal potential can be omitted. The remainder of the differential centrifugal potential is called the pole tide potential, which is only a function of the location of the instantaneous rotation pole. If the arbitrary point $\vec{r} = (x, y, z)$ is expressed in geographical coordinates (colatitude θ and longitude λ), the pole tide potential is then expressed as

$$\begin{cases} V(r, \theta, \lambda, t) = -\dfrac{r^2\Omega^2}{2}(m_1(t)\cos\lambda + m_2(t)\sin\lambda)\sin 2\theta \\ \vec{r} = (r, \theta, \lambda) \end{cases} \tag{4}$$

3. The theoretical gravity pole tide

The gravity change caused by the pole tide potential is given by the following formula [Wahr 1985; Huang C. L. 1998; Xu J. Q. 2004],

$$\Delta g(\theta, \lambda, t) = \delta \cdot r \cdot \Omega^2 (m_1(t)\cos\lambda + m_2(t)\sin\lambda)\sin 2\theta \tag{5}$$

where r is usually taken as the mean radius of the Earth, $r = a$ =6378136.6 m. The value of δ is 1.0 for a rigid Earth, and about 1.16 for a spherical elastic Earth. The theoretical gravity pole tide is calculated with formula (5) with the value δ=1, that is for a rigid Earth. The instantaneous pole tide coordinates $m_1(t)$ and $m_2(t)$ are computed from the observed values $x(t)$ and $y(t)$ which are defined in a celestial ephemeris coordinate system. They are expressed in the form of complex notation [Gross 1992].

$$\begin{cases} \mathbf{p}(t) = x(t) - i \cdot y(t) \\ \mathbf{m}(t) = m_1(t) + i \cdot m_2(t) = \mathbf{p}(t) - \dfrac{i}{\Omega}\dot{\mathbf{p}}(t) \end{cases} \tag{6}$$

The transformation from **p** (t) to **m** (t) is used to eliminate the drift of the mean pole.

The observed instantaneous pole tide coordinates $x(t)$ and $y(t)$ are downloaded from the International Earth Rotation Service (IERS). We choose a time period January 1, 1995 to December 31, 1999, when the amplitude of the theoretical gravity pole tide covers almost its total range, in order to see the corresponding characteristic of the gravity loading effect of the ocean tide. The bold lines in Figure 1 and Figure 2 show the theoretical gravity pole tide at station Brussels.

4. The classical and the self-consistent equilibrium ocean pole tide

The classical equilibrium ocean pole tide $\zeta_O^C(\theta,\lambda,t)$ of an arbitrary point $r(a,\theta,\lambda)$ can be computed by the following equation [Desai, 2002].

$$\begin{cases} \zeta_O^C(\theta,\lambda,t) = \gamma_2\left[\dfrac{8\pi}{15}\right]^{\frac{1}{2}} \dfrac{\Omega^2 a^2}{g} \cdot \mathrm{Re}\left[\mathbf{m}^*(t)\cdot \overline{E}^C(\theta,\lambda)\right] \\ \overline{E}^C(\theta,\lambda) = O(\theta,\lambda)\left[\overline{P}_{21}(\cos\theta) + K^C\right] \end{cases} \tag{7}$$

where $\gamma_2 = \bar{\gamma}_2 \exp\left(i\cdot\Delta\varphi^C\right)$, is the Love number related to the ocean tide. $\Delta\varphi^S$ denotes the phase lag between the classical equilibrium ocean pole tide and the static ocean tide, $\bar{\gamma}_2$ =0.7053. The mean gravitational acceleration at the Earth's surface g has been substituted with the ratio GM/a^2 in the calculation, where GM is the Earth's gravitational constant, GM =3.9860004418×10^{14} m^3·s^{-2}. The complex constant K^C is introduced to impose the conservation of mass on the classical equilibrium ocean pole tide. $\overline{E}^C(\theta,\lambda)$ is defined as a normalized equilibrium admittance function for the classical equilibrium ocean pole tide, so that the mass conservation can be done easily and the computation is then independent of the time. The ocean function $O(\theta,\lambda)$ has value of 1 on the ocean and 0 on the land [Muck and Macdonald, 1960]; the boundary of the ocean and the land used in the calculation is the boundary defined in ocean tide model NAO99 [Matsumoto 2000].

The self-consistent equilibrium ocean pole tide $\zeta_O^S(\theta,\lambda,t)$ of an arbitrary point $r(a,\theta,\lambda)$ can be computed by the following equation [Desai, 2002].

$$\begin{cases} \zeta_O^S(\theta,\lambda,t) = \gamma_2\left[\dfrac{8\pi}{15}\right]^{\frac{1}{2}} \dfrac{\Omega^2 a^2}{g} \cdot \mathrm{Re}\left[\mathbf{m}^*(t)\cdot \overline{E}^S(\theta,\lambda)\right] \\ \overline{E}^S(\theta,\lambda) = O(\theta,\lambda)\left[\overline{P}_{21}(\cos\theta) + \sum_{n=0}^{\infty} \gamma_n' \alpha_n \overline{E}_n^S + K^S\right] \end{cases} \tag{8}$$

where the Love number γ_2 is also assumed with the complex form, $\gamma_2 = \bar{\gamma}_2 \exp\left(i\cdot\Delta\varphi^S\right)$, but $\Delta\varphi^S$ denotes the phase lag between the self-consistent equilibrium ocean pole tide and the static ocean tide. The complex constant K^S is also introduced here to impose the conservation of mass on the self-consistent equilibrium ocean pole tide. $\overline{E}^S(\theta,\lambda)$ is defined as a normalized equilibrium admittance function for the self-consistent equilibrium ocean pole tide. The second term in the square brackets of $\overline{E}^S(\theta,\lambda)$ describes the effects of tidal loading and self-gravitation of the ocean pole tide, where γ_n' is load Love number of degree n and α_n is the factor $(3/(2n+1))\,(\rho_w/\rho_e)$, ρ_w and ρ_e define the mean densities of the ocean water and the Earth, respectively, with $(\rho_w/\rho_e)\approx 0.19$ [Munk and MacDonald 1960]. The function $\overline{E}^S(\theta,\lambda)$ can be expanded into spherical harmonic components defined by coefficients $(a_{nm} + i\cdot b_{nm})$. We obtained the spherical harmonic coefficients from Desai by personal communication. And the coefficients given by Desai are expanded to degree

n =360, which implies a spatial resolution of 0.5 degrees in latitudes and longitude.

$$\overline{E}^{S}(\theta,\lambda)=\sum_{n=0}^{\infty}\sum_{m=-n}^{n}\overline{P}_{n|m|}(\cos\theta)(a_{nm}+ib_{nm})e^{im\lambda} \tag{9}$$

5. Gravity loading effect of the equilibrium ocean pole tide

The gravity loading effect of the equilibrium ocean tide $L(\theta,\lambda,t)$ at a given time t can be calculated by a convolution [Agnew 1997; Zhou J. C. 2005]

$$L(\theta,\lambda,t)=\rho_w a^2\iint_{S_O}H(\theta',\lambda',t)G(\psi)\sin\psi\,d\psi\,dA \tag{10}$$

where $H(\theta',\lambda',t)$ is the height of the ocean tide at the point of the colatitude θ' and the longitude λ' at the corresponding time. And $G(\psi)$ is the Green's function; A is the azimuth from the selected point (θ,λ) and the loading point (θ',λ'); $\psi\in[0,\pi]$ is the angular distance between the selected point (θ,λ) and the loading point (θ',λ'), given by the formula.

$$\cos\psi=\cos\theta\cos\theta'+\sin\theta\sin\theta'\cos(\lambda-\lambda') \tag{11}$$

As an example, we calculate the gravity loading effects of the classical and the self-consistent ocean pole tide at station Brussels. Figure 1 shows the comparison with the theoretical gravity pole tide before (a) and after (b) introducing a well-chosen phase lag. From Figure 1 (a) we can see that the amplitude of the gravity loading effect of the self-consistent ocean pole tide is larger than that of the classical ocean pole tide, the amplitude of both of them being larger than 10^{-9} m.s^{-2}. There is a slight but noticeable phase shift between ocean pole tide loading and the theoretical gravity pole tide in Brussels. From Figure 1 (b) we can see that the difference of the amplitude between the loading effect of the self-consistent ocean pole tide and that of the classical ocean pole tide decreases slightly; when the phase shift is corrected.

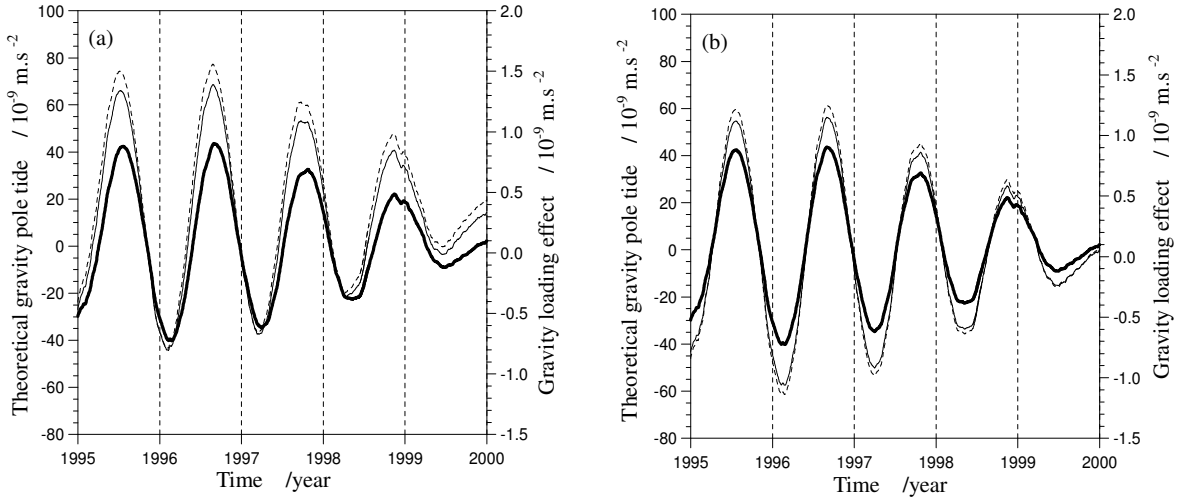

Figure 1 Comparison of the theoretical gravity pole tide and the gravity loading effects of the ocean pole tide before (a) and after (b) introducing a well-chosen phase lag. The bold line is the theoretical gravity pole tide; the fine line is the gravity loading effect of the classical equilibrium ocean pole tide; the dashed line is the same effect of the self-consistent equilibrium ocean pole tide

The gravity loading vector takes the complex forms $\vec{\delta}_L=\delta_L\cdot e^{i\Delta\varphi_L}$, where δ_L is the amplitude and $\Delta\varphi_L$ refers to the phase difference. Lags correspond to negative values. The estimation of the gravity loading vector is

based on the assumption that the theoretical gravity pole tide $\Delta g(\theta,\lambda,t)$ and the gravity loading effect of the ocean tide $L(\theta,\lambda,t)$ at a given point (θ_0,λ_0) has the relationship shown in the following equation.

$$L(\theta_0,\lambda_0,t)=\vec{\delta}_L\cdot\Delta g(\theta_0,\lambda_0,t)=\delta_L\cdot e^{i\Delta\varphi_L}\cdot\Delta g(\theta_0,\lambda_0,t) \tag{12}$$

The assumption is reasonable, as it can be seen from Figure 2 and Figure 3. Figure 2 shows the phasor plot of the gravity loading effect of the classical equilibrium ocean pole tide and the theoretical gravity tide of station Brussels, before and after introducing the phase difference. Figure 3 corresponds to Figure 2 for the self-consistent equilibrium ocean pole tide. From Figure 2 and Figure 3, we can see that phasor plot of the gravity loading effects with respect to the theoretical gravity looks like an ellipse for both the classical and the self-consistent ocean pole tide. After introducing a well-chosen phase difference, it can be completely fitted by a straight line. Therefore, we can conclude that the assumption in equation (8) is correct. If the linear fit takes the form $Y = AX + B$, the coefficient A of the linear fit is the amplitude factor of the loading gravimetric vector. The well-chosen phase difference is the phase of the loading gravimetric vector.

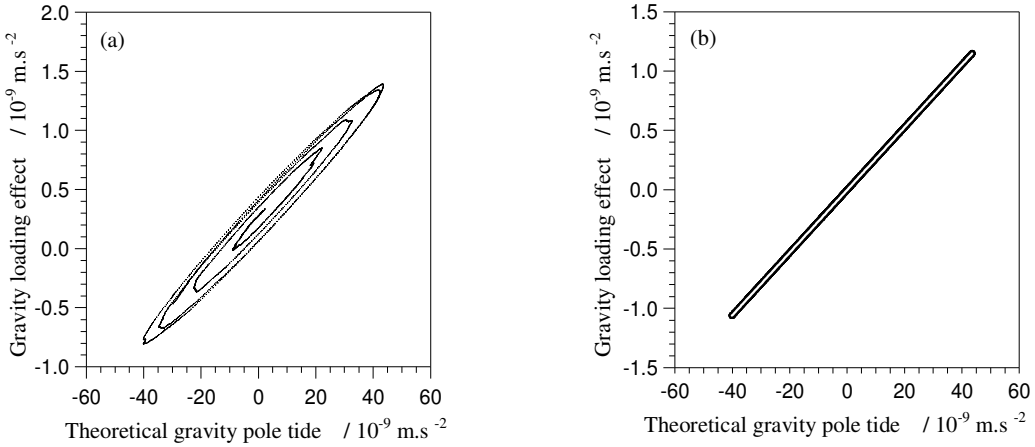

Figure 2: Linear fit of the gravity loading effect of the classical equilibrium ocean pole tide and the theoretical gravity tide of station Brussels, before (a) and after (b) introducing a well-chosen phase lag. The white straight line in (b) is the fit line.

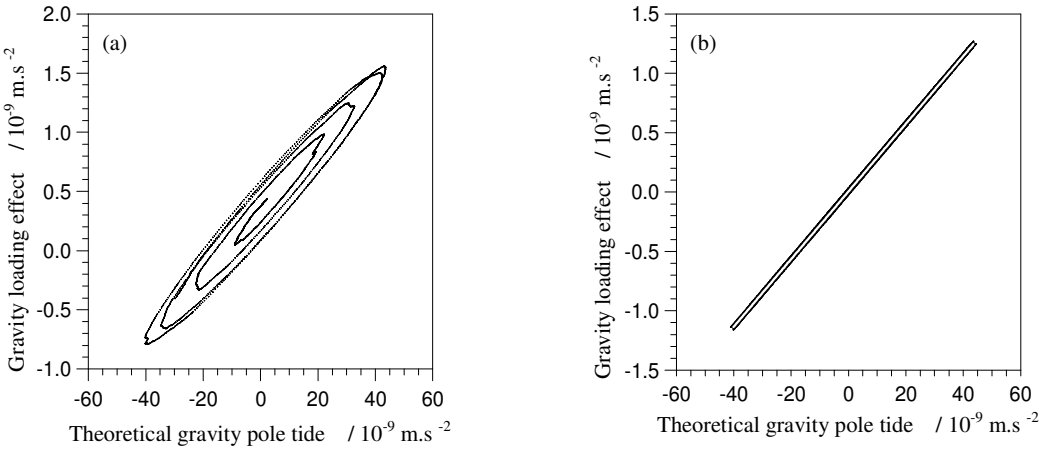

Figure 3: Linear fit of the gravity loading effect of the self-consistent equilibrium ocean pole tide and the theoretical gravity tide of station Brussels, before (a) and after (b) introducing a well-chosen phase lag. The white straight line in (b) is the fit line.

The loading gravimetric vectors of all the other GGP stations are obtained with the same method. The numerical result for 9 stations is given in the Table 1. From table 1, we can see that the largest amplitude of

loading gravimetric vectors is the amplitude of Canberra, The amplitude factor value is 0.0363 for the classical model and 0.0429 value for the self-consistent one. The reason we considered is that the station Australia is surrounded by the oceans. The smallest amplitude of loading gravimetric vectors is found at Boulder, The amplitude factor value is 0.0137 for the classical model and 0.0152 value for the self-consistent one. The reason is that the station Boulder lies in the inner part of the North America mainland and is far away from the ocean. The mean value for all the stations is 0.0224 for the classical model and 0.0247 for the self-consistent one. Compared with the theoretical value of the gravimetric factor δ=1.158 for a non-hydrostatic and anelastic Earth model given by Dehant in 1999, these two mean values correspond to 1.9% and 2.1%, respectively [Dehant et al., 1999]. Therefore, the influence of the ocean pole tide cannot be omitted when we try to determine the gravimetric factor δ with gravity observations. The largest phase difference is found at station Vienna, an advance of 12.10 days for the classical ocean pole tide and of 15.55 days for the self-consistent one. The smallest phase difference is the phase advance of Boulder too, 4.32 days for the classical ocean pole tide and 4.75 days for the self-consistent one. Phase lags are observed in Canberra and Cantley. However it should be noted that, as the load vectors represents 2% of the direct gravity pole tide, a 10° phase shift will only produce a 0.2° phase difference on the observed gravity pole tide. Considering the results of Ducarme et al. [2006] it is, for the while at least, below the limit of detection. Compared to the preliminary evaluations given in Ducarme et al. [2006] there is an increase of the tidal loading of the order of 30%. The mean corrected tidal factor should become δ=1.156 for the classical ocean pole tide model and δ=1.154 with the self-consistent one. However the RMS error on the mean tidal gravity amplitude factor is still at the 0.5% level so that both values agree with the value δ=1.158 of the DDW99 model [Dehant et al., 1999].

Table 1: Loading gravimetric vectors of 9 GGP stations

Station	Loading gravimetric vector (classical)			Loading gravimetric vector (self-consistent)		
	Amplitude factor δ_L	Phase diff. at 435day (°)	Time shift (day)	Amplitude factor δ_L	Phase diff. at 435day (°)	Time shift (day)
Boulder	0.0137	3.60	4.32	0.0152	3.96	4.75
Brussels	0.0264	7.20	8.64	0.0285	9.00	10.80
Canberra	0.0363	-3.24	-3.89	0.0429	-4.14	-4.97
Cantley	0.0210	-8.46	-10.15	0.0236	-9.36	-11.23
Membach	0.0242	8.10	9.72	0.0261	9.90	11.88
Moxa	0.0201	9.90	11.88	0.0217	12.24	14.69
Potsdam	0.0210	9.54	11.45	0.0223	11.88	14.26
Strasbourg	0.0214	8.64	10.37	0.0233	10.80	12.96
Vienna	0.0174	10.08	12.10	0.0186	12.96	15.55
Mean value	0.0224	---	---	0.0247	---	---

6. Conclusions

The amplitude of the loading gravity effect of the ocean pole tide is of the level of 10^{-9} ms^{-2}, and its phase difference with respect of the gravity pole tide ranges between -11 and +16 days. This loading effect can increase the amplitude factor of gravity the pole tide by more than two percent, but its effect on the phase remains negligible. The self-consistent model predicts effects 10% larger than the classical one.

Reference

1. Agnew D. C., Farrell W. E., *Self-consistent equilibrium ocean tides*. Geophys. J. R. astr Soc., 1978, 55: 171 – 181

2. Agnew D. C., *NLOAF: A program for computing ocean-tide loading*, J. Geophys. Res., 1997, 102(B3): 5109 – 5110.
3. Boy J. P., Hinderer J., Amalvict M., Calais E. *On the use of the long records of superconducting and absolute gravity observations with special application to the Strasbourg station, France*, the European Centre for Geodynamics and Seismology, 2000, 17: 67 – 83.
4. Crossley D., Hinderer J., Casula G., Francis O., Hsu H. T., Imanishi Y., Jentzsch G., Kääriäinen J., Merriam J., Meurers B., Neumeyer J., Richter B., Shibuya K., Sato T., Van Dam T., *Network of superconducting gravimeters benefits a number of disciplines*, EOS, 1999, 80(11): 121 – 126
5. Dehant V., Defraigne P, Wahr J. *Tides for a convective Earth*. J Geophys Res, 1999, 104, B1, 1035-1058
6. Dehant V., Zschau J., *The effect of mantle inelasticity on tidal gravity: a comparison between the spherical and the elliptical earth model*, Geophysical Journal, 1989, 97: 549-555
7. Dahlen F. A., *The passive influence of the oceans upon the rotation of the Earth*, Geophys. J. R. astr. Soc., 1976, 46: 363 – 406
8. Desai S. D., *Observing the pole tide with satellite altimetry*, J. Geophys. Res., 107(C11), 3186, doi:10.1029/2001JC001224, 2002.
9. Dickman S. R., *The self-consistent dynamic pole tide in global oceans*, Geophys. J. R. astr. Soc, 1985, 81: 157 – 174.
10. Ducarme, B., Venedikov, A.P., Arnoso, J., Vieira, R., Chen X.D., Sun H.P., *Global analysis of the GGP superconducting gravimeters network for the estimation of the polar motion effect on the gravity variations.* , Proc. 15th Int. Symp. On Earth Tides, Ottawa, August 2-6, 2004. J. Geodynamics, 2006, 41, 334 – 344.
11. Gross R. S., *Correspondence between theory and observations of polar motion*, Geophys. J. Int. 1992, 109: 162 – 170.
12. Harnisch M., Harnisch G., *Study of long-term gravity variations, based on data of the GGP Co-operation, a continuation*, Proc. 15th Int. Symp. On Earth Tides, Ottawa, August 2-6, 2004. J. Geodynamics, 2006, 41: 318 – 325.
13. Haubrich R. and Munk W. H., The pole tide, J. Geophys. Res., 1959, 64: 2373 – 2388.
14. Hinderer, J. & Legros, H., *Elasto-gravitational deformation, relative changes in gravity and earth dynamics*, Geophys. J., 1989, 97, 481-495.
15. Huang C. L., Ducame B., Jin W. J., O*n the possibility of detecting a signal of the earth rotation with gravimetry*, Marees Terrestres Bulletin d'Information (BIM), 1998, 129: 9974 – 9981.
16. Lambeck K., *Geophysical Geodesy: The Slow Deformation of the Earth*, Oxford Univ. Press, New York, 1988.
17. Loyer S., Hinderer J., Boy J. P., *Determination of the gravimetric factor at the Chandler period from Earth orientation data and superconducting gravimetry observations*, Geophys. J. Int. 1999, 136: 1 – 7.
18. Matsumoto K., Takanezawa T. and Ooe M., *Ocean tide models developed by assimilating TOPEX/ POSEIDON altimeter data into hydrodynamical model: a global model and a regional model around Japan*, J. Oceanography, 2000, 56: 567 – 581.
19. Munk W. H. and Macdonald J. F., *The Rotation of the Earth: A Geophysical Discussion*, Cambridge Univ. press, New York, 1960.
20. Naito I., *Effects of the pole tide on the Chandler Wobble*, J. Phys. Earth, 1979, 27: 7 – 20.
21. Naito I., *Responses of the ocean to the Chandler Wobble*, Mar. Geod., 1983, 7: 345 – 358.
22. O'Connor W. P., Starr T. B., *Approximate particular solutions for the pole tide in a global ocean*, Geophys. J. R. astr. Soc., 1983, 3: 244 – 249.
23. Proudman J., *The condition that a long-period tide shall follow the equilibrium law*, Geophys. J. R. astr. Soc.,1960,3: 244 – 249.
24. Wahr J. M., *Deformation induced by polar motion*, J. Geophys. Res., 1985, 90(B11): 9363 – 9368.
25. Wunsch C., *Dynamics of the pole tide and the damping of the Chandler wobble*, Geophys. J. R. astr. Soc., 1974, 39: 539 – 550.
26. Xu J. Q. Sun H. P., Yang X. F., *A study of gravity variations caused by polar motion using superconducting gravimeter data from the GGP network*, J. Geodesy, 2004, 78: 201 – 209.
27. Zhou J. C., Sun H. P., *Influence of the modified global ocean tide model with local tides of East and South China Seas on load gravity in China and its neighbor area*, ACTA SEISMOLOGICA SINICA, 2005, 18(3): 354 – 360.

A search on the gravity / height ratio induced by surface loading; theoretical investigation and numerical applications

Caroline de Linage*, Jacques Hinderer & Jean-Paul Boy
EOST/IPGS (UMR 7516 CNRS/ULP), 5 rue René Descartes, 67084 Strasbourg, France
* E-mail : Caroline.De-Linage@eost.u-strasbg.fr

Introduction

Ground gravity measurements are very often collocated with measurements of surface vertical displacements. These two observables are due to deformation processes acting on different spatio-temporal scales. Combining them through a ratio may provide useful information about the physics of the acting phenomena and help to separate various contributions. A well-known theoretical value of such a ratio is the free-air gradient of -0.3086 μGal/mm used in the free-air reduction. However, because of the redistribution of the masses inside the Earth and the Newtonian attraction, this ratio for surface loading is different from the free-air gradient. For example, Wahr et al. (1995) showed that the viscous vertical displacement could be linked to the corresponding free-air gravity anomaly via a coefficient of 6.5 mm/μGal or, equivalently, that the secular variation of the total gravity could be linked to the secular vertical displacement through a ratio of -0.15 μGal/mm. This value should be constant whatever the viscosity profile inside the compressible Earth, the ice geometry and time history, as shown theoretically and numerically. These authors proposed to use this ratio to separate the effects of Present-Day Ice Melting (PDIM) from those of Post Glacial Rebound (PGR).
In this study, we aim at probing the characteristics of gravity versus vertical displacement (gravity/height) ratio in the case of an elastic loading process. We first investigate theoretically the ratio to better understand the sensitivity of its different components to the spatial wavelengths of the source (part 1). We develop a numerical approach for computing this ratio and apply it to the predictions of the hydrological loading using a global hydrological model (part 2).

1 Theoretical study of the gravity/height ratio

The theory of the loading process is considered by Farrell (1972) and Merriam (1980) for oceanic loading, and by Spratt (1982) for atmospheric loading.
The variation T of a geodetic observable at the location (θ, λ) induced by a variation of a 2D mass distribution σ(θ, λ) at the Earth's surface can be written as:

$$T(\theta,\lambda) = \sum_{n=0}^{+\infty} \tau_n \sum_{m=0}^{n} P_n^m(\cos\theta)\left(\sigma_n^{m,c}\cos(m\lambda) + \sigma_n^{m,s}\sin(m\lambda)\right) = \sum_{n=0}^{+\infty} \tau_n\, \sigma_n(\theta,\lambda)$$

where τ_n is the transfer function of degree n for the observable T. In our study T stands for gravity variation or vertical displacement.

The transfer function depends on the elastic properties of the Earth via the load Love numbers. The Earth model that is used is the Spherically Symmetric, Non-Rotating Elastic and Isotropic (SNREI) compressible Earth model PREM without oceans.

1.1 Gravity and vertical displacement induced by a 2D mass distribution at the Earth's surface

We now examine the degree n term of the transfer function in gravity (g_n) and vertical displacement ($u_{r,n}$).

1.1.1 Gravity variation

By convention, gravity is positive downwards. The gravity variation can be decomposed into a Newtonian and an elastic part.
The Newtonian part of the transfer function can be written as (Merriam, 1980) (ρ_T is the mean density of the Earth):

$$g_{N,n} = -\frac{3\,g_0}{R_T\,\rho_T}\frac{n}{2n+1} \tag{1}$$

or

$$g_{N,n} = -\frac{3\,g_0}{R_T\,\rho_T}\frac{-(n+1)}{2n+1} \tag{2}$$

depending on the location of the very local masses (resp. above (eqn. 1) and below the measurement point (eqn. 2)). Although there is an impact of the masses at global scale, gravity is dominated by the effect of these masses via the Dirac term in the Green function (Merriam, 1980). The limit when n tends to infinity is resp. $-2\pi G$ (masses above) and $+2\pi G$ (masses below) corresponding to the gravity effect of infinite plate of density σ ($\pm$ 0.042 µGal/(kg/m²)).
The elastic part of the transfer function can be written as (Merriam, 1980):

$$g_{E,n} = -\frac{3\,g_0}{R_T\,\rho_T}\frac{2\,h'_n-(n+1)k'_n}{2n+1} \tag{3}$$

The two components in this expression are:

- the effect of free-air motion (h'_n term)
- the effect of the mass redistribution inside the Earth (k'_n term)

These two components are opposite in sign. Their sum is positive and tends to zero when n tends to infinity. It decreases (resp. increases) the sensitivity to low degrees if the local masses are below (resp. above) the surface.

Hence ground gravity is sensitive to the entire spectrum of the source (through the Newtonian term).

1.1.2 Vertical displacement

By convention, vertical displacement is positive upwards. The reference frame is centered at the center of mass of the system {Earth + load}.
The degree n term of the transfer function can be written as (Farrell, 1972):

$$u_{r,n} = \frac{3}{\rho_T}\frac{1}{2n+1}h'_n \tag{4}$$

This transfer function is a decreasing function of the degree n and tends to zero when n tends to infinity. Hence vertical displacement is mainly sensitive to the lowest degrees (inferior to 20) of the source and behaves as a low-pass filter. Thus a load of small spatial extension will induce almost no vertical displacement.

1.2 Ratio of the degree n terms of the transfer functions or Green functions

A way to compare the different sensitivities of the transfer functions for gravity and displacement (or Green functions) is to compute the ratio of their degree n terms. Because the ratio is not a linear function of the source, it is not the transfer function for the gravity/height ratio. So the ratio of the degree n terms of the transfer functions has not to be interpreted as the degree n term of the gravity/height ratio.

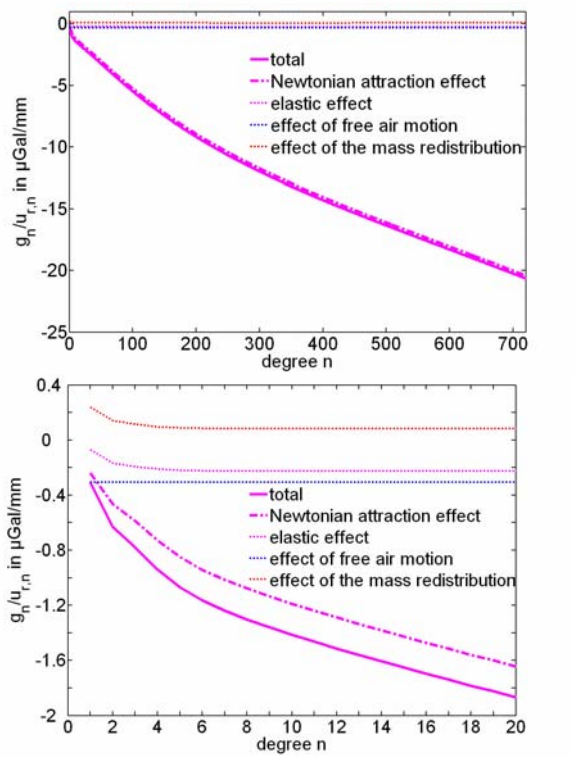

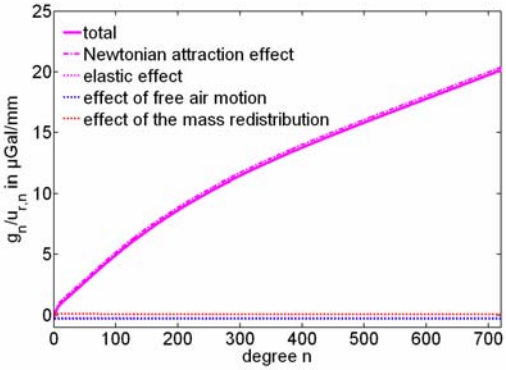

Figure 1. Ratio g_n/u_{rn} of the degree n terms of the transfer functions in gravity and vertical displacement. Left (top): local masses below the surface; zoom on the first 20 degrees (left bottom). Right (top): local masses above.

As shown on Figure 1, the ratio is dominated by the Newtonian attraction term due to the local masses (magenta full line) which determines its sign (depending on the location of the very local masses). It corresponds to the ratio of equations (1) or (2) to equation (4). Since vertical displacement tends to zero when n tends to infinity, the ratio diverges rapidly.
This constitutes a strong limitation in the interpretation of the gravity/height ratio. Because of the location of the gravimeters with respect to the ground, the sign of the gravity variations due to hydrology can be opposite as well as the sign of the ratio.
It is interesting to focus on the ratio of the elastic part of gravity to vertical displacement (magenta dotted curves) because of their similar behavior as a function of the degree of the source. It can be written as follows (equation (3) divided by equation (4)):

$$\frac{g_{E,n}}{u_{r,n}} = -\frac{g_0}{R_T}\frac{2h'_n - (n+1)k'_n}{h'_n} = -\frac{2g_0}{R_T} + \frac{g_0}{R_T}\frac{(n+1)k'_n}{h'_n} \qquad (5)$$

The first term (blue dotted line) is the famous free-air gradient whose value for a spherical Earth is -0.3086 μGal/mm. Since it is not dependent on the degree n, this value can be used in the spatial domain to correct gravity variations from the free-air motion effect.
The second term (red dotted line) is due to the mass redistribution inside the Earth which partly compensates the deformation of the surface. It tends rapidly to a limit when n tends to infinity.
The limit of both terms (computed at degree n=9000) is equal to -0.2320 μGal/mm. This value may explain smaller absolute values of the gravity/height ratio far away from the loads, as the local Newtonian effect is then equal to zero.

1.3 Generalization to any load

Real loads are not constituted by one single degree but by a long series of degrees in order to reproduce their complex spatial geometry such as the hydrological basin limits or the ocean-continent limit.
At the location (θ, λ), the gravity/height ratio is then the ratio of two combinations of degrees, characterized by two different transfer functions:

$$\frac{g(\theta,\lambda)}{u_r(\theta,\lambda)} = \frac{\sum_{n=0}^{+\infty} g_n \, \sigma_n(\theta,\lambda)}{\sum_{n=0}^{+\infty} u_{r,n} \, \sigma_n(\theta,\lambda)}$$

We consider now a load whose spatial distribution changes with time:

$$\sigma(\theta,\lambda,t) = \sum_{n=0}^{+\infty} \sigma_n(\theta,\lambda,t)$$

Since generally the geometry of the load is not the same according to time, we cannot separate time and space dependencies and the gravity/height is time-dependent (however in the case of tidal waves of fixed frequency, it is possible to make such a separation by considering the ratio as a complex number with an amplitude in μGal/mm and a phase).

2 Numerical study of the gravity/height ratio

As shown above, the ratio gravity/height is a complex function of space and time. It may diverge at some time t or location (θ, λ) because of a vanishing vertical displacement.

2.1 Methodology

At a point (θ, λ), we first compute a gravity/height ratio for a given period of time D by a linear regression using the least squares method (Figure 2). Time is thus removed. This method avoids taking into account abnormally large values of the ratio as it would be the case by computing the arithmetical mean. However, a shortcoming of this method is that it fails to give the right ratio if gravity and vertical displacement are not in phase (case of tidal waves).

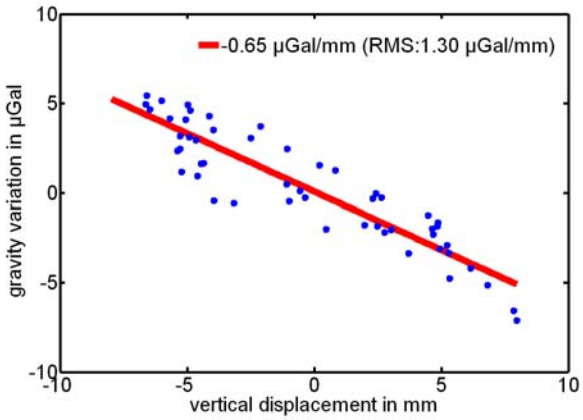

Figure 2. Linear regression between vertical displacement and gravity variation in Strasbourg predicted by the global hydrological LaD model (Milly & Shmakin, 2002). Each blue dot represents a monthly time sample.

A second step is the computation of the spatial mean of the ratios calculated as explained above on a given domain (continents, hydrological basins).
We could also make a global linear regression removing both time and space. So we compared the resulting ratio to the one obtained by the former method and found very close values. However, the spatial integration of such a ratio is not meaningful on a global scale but rather on smaller domains we will identify below.

2.2 Application to a global hydrological model

We use the global LaD model from Milly & Shmakin (2002) given with a temporal sampling of one month on a 1° square grid. The investigated time period ranges from January 2000 to April 2004. We use the predictions of snow cover and soil moisture (as sum of the water in the root zone and ground water). The Root Mean Square (RMS) of the temporal variations for each quantity and their sum are mapped in Figure 3.
In glaciated areas such as Antarctica and Greenland, the model fails to give realistic values of snow cover (too much accumulation of snow) so we removed their contribution to global hydrological loading.

Areas with a strong signal are located in the equatorial zone where strong precipitations occur especially during the monsoon. The corresponding hydrological basins are Orinoco, Amazon and Tocantins basins in South America, Niger, Chad and Congo basins in Africa and Brahmaputra and Mekong basins in South East Asia.
It should be reminded that there is a phase-lag of 6 months because of the meteorological equator. Thus the Orinoco and Amazon basins are not in phase and so are the Chad and Congo basins. As a consequence, the effective loads are smaller than those showed on Figure 3.
In Europe, the signal is not so strong than in the equatorial area but is coherent on a large scale. It is due only to the variations of water contained in the soil.
In Russia and particularly in Siberia, the predicted variations of snow cover dominate the total signal which is stronger than the one predicted in Amazon.
In the northern part of the country, the model predicts a strong signal related to high precipitations whereas almost no signal is predicted for the rest of the country.

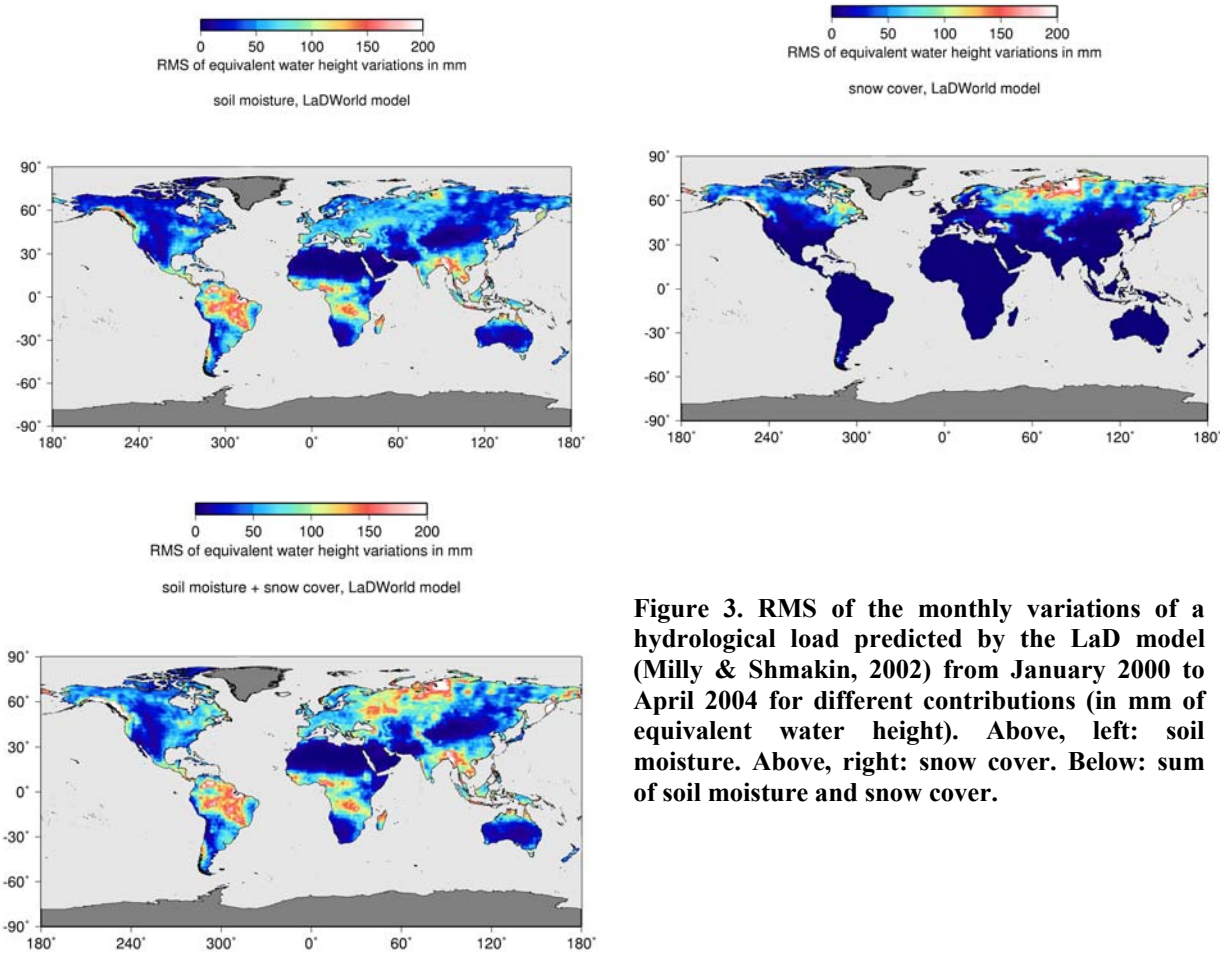

Figure 3. RMS of the monthly variations of a hydrological load predicted by the LaD model (Milly & Shmakin, 2002) from January 2000 to April 2004 for different contributions (in mm of equivalent water height). Above, left: soil moisture. Above, right: snow cover. Below: sum of soil moisture and snow cover.

The spectral energy of the variations of the total hydrological load (Figure 4) is maximum around degree 5 corresponding to a spatial half wavelength of 4000 km. However the ocean-continent limit introduces other degrees and the load cannot be assumed as a pure degree 5. Moreover the distribution of energy as a function of degree is changing with time.
The two peaks per year (around March and September) correspond to the annual cycle which is out of phase of 6 months between the Northern and Southern hemispheres.

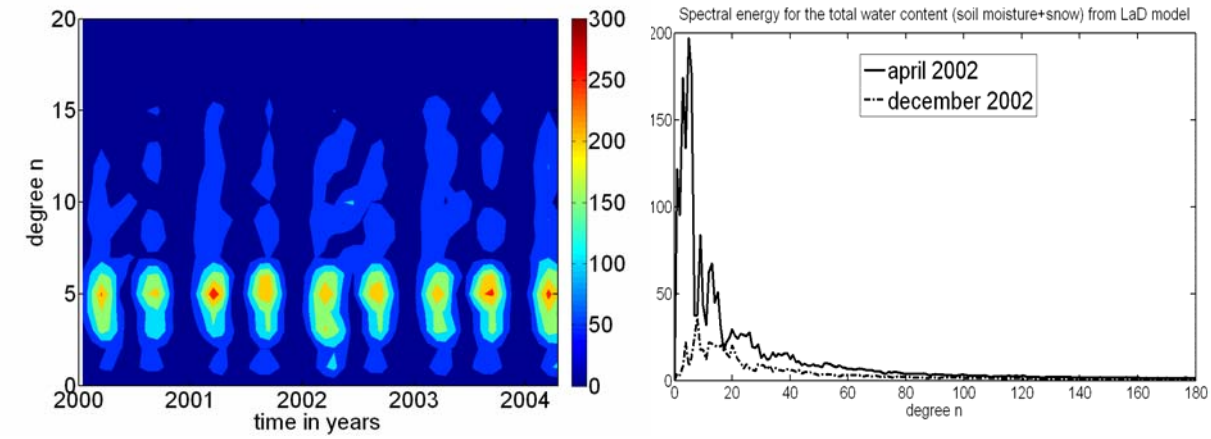

Figure 4. Spectral energy (in mm²) of the predicted total water content (soil humidity and snow cover) by LaD model versus degree and time (left) and versus degree at two different months (right).

2.3 Results

For the computation of gravity variations induced by these water content variations, we assume that the local masses are below the measurement point by using equation (2) for the Newtonian attraction effect. The 1° square grid has been interpolated to 0.5°. We truncated the development of equations (2) to (4) at degree 360.
The gravity/height values computed for each (θ, λ) point as explained in part 2.1 are mapped on Figure 5.

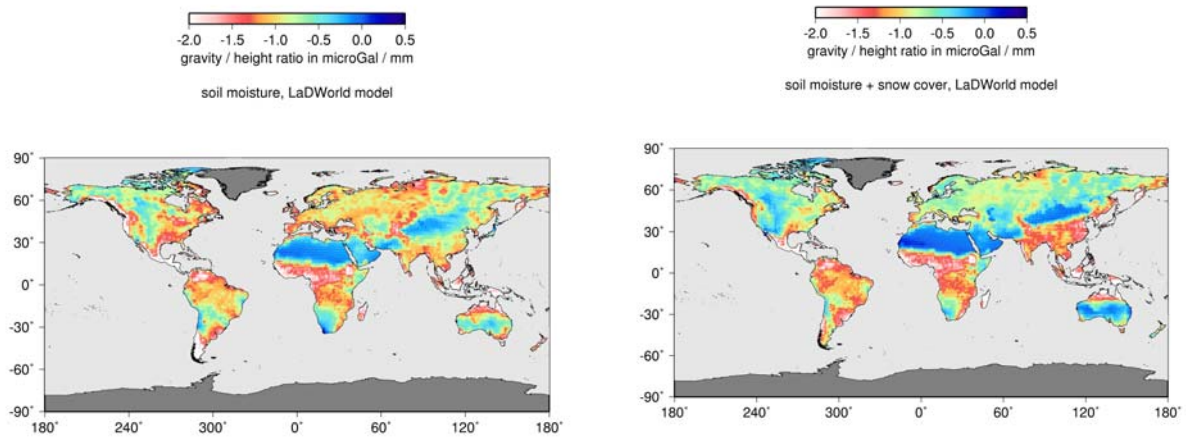

Figure 5. Gravity/height ratio in µGal/mm for the global hydrology model LaD. Left: effect of soil moisture. Right: effect of total water content (soil moisture and snow).

2.3.1 Effect of snow

We computed separately the gravity/height ratio for snow cover and soil moisture effects. Since the predicted snow cover variations present a strong degree 1, it will have an impact on the ratio even far away from the sources as shown on Figure 5.
For example, the mean ratio computed in Europe (area between -10°E and 35°E in longitude and between 35°N and 75°N in latitude) is -1.03 µGal/mm if we consider only the soil moisture variations and increases to -0.71 µGal/mm if the snow cover variations are considered besides those of soil moisture.
This can be explained in two steps. On one hand, gravity is almost not affected because there is no (or negligible) snow in Europe so that the local Newtonian attraction effect is almost zero. On the other hand, snow cover in Siberia causes a flexure of the crust and therefore a vertical displacement which adds to the vertical displacement caused by soil moisture in Europe.

2.3.2 Spatial variations of the gravity/height ratio

The mean value of the ratio induced by soil moisture and snow cover variations is -0.86 µGal/mm but the RMS on the continents is 0.57 µGal/mm. The ratio ranges from -6.4 µGal/mm to 1.8 µGal/mm and only 0.6% of the computed values are inferior to -2.0 µGal/mm indicating that the mean ratio is not affected by too high values.

2.3.2.1 Comparison of the means on different hydrological basins

If we compare Figure 5 with Figure 3, we cannot find everywhere a correlation between a high signal and a high (in absolute value) gravity/height ratio. It is due to temporal phase lags between basins that are not shown in Figure 3. For example, as already mentioned in part 2.2, there is a phase lag of 6 months between the Orinoco and the other basins of South America. The latter add their effects to the loading of the area inducing a significant vertical displacement. But the Orinoco basin being smaller, the induced vertical displacement is not so important. Then, gravity variations being comparable in both areas, the gravity/height ratio is higher in Orinoco basin (-1.38 μGal/mm) than in the other basins of South America (-1.11μGal/mm).
In Northern Australia (latitudes below 20°S), the value is -1.84 μGal/mm which is twice the mean value. This is due to the small spatial extension of the source which results in a small vertical displacement and a big gravity change. It is also the case in every island where there is a significant hydrological signal and on the Western coast of Canada where the signal is concentrated on a narrow area.
In Siberia, however, the mean value is -0.82 μGal/mm although the predicted signal is one of the highest in the world.
So the gravity/height ratio does not automatically depend on the amplitude of the load, but it is closely influenced by its spatial extension. Thus, the more concentrated the source is, the smaller the vertical displacement and the higher the ratio.

2.3.2.2 Case of desert areas (outside the loads)

We are now considering the impact of soil moisture only (Figure 5, left).
We find a mean value of -0.28 μGal/mm in the area formed by Sahara and Arabia (latitudes between 15°N and 30°N).
Close values can also be found in Central Asia (Mongolia), and Central Australia.
In these areas, as shown in Figure 3, there is no hydrological signal. However, gravity variations and vertical displacements are not zero. In gravity, the Newtonian attraction part is indeed zero and only the elastic part and the global Newtonian attraction effect are non zero. The vertical displacement is not zero because of the bending of the crust induced by the strong hydrological signal in the African equatorial zone.
We do not find -0.23 (limit value of equation (5), part 1.2) because of the small global Newtonian attraction effect which enhances the effect in gravity.

Conclusion

The gravity/height ratio is strongly dominated by the effect in gravity of the Newtonian attraction of the local masses (Dirac effect) as its sign depends on the position of the local masses. The elastic effect due to mass redistribution inside the Earth and free-air motion (via the -0.3086 μGal/mm value) is much smaller and is not so sensitive to the degree n of the source. It leads to a ratio more or less close to -0.23 μGal/mm.
Numerical application for a predicted global hydrological load gives a mean ratio of -0.86 μGal/mm. This value was found by first using a linear regression through time at any continental point and then computing a spatial mean over the continents. However, the different mean values found on several hydrological basins are mainly controlled by the basin size; the more concentrated the source is, the smaller the vertical displacement and the higher the gravity/height ratio.

On the contrary, in desert areas, the ratio is dominated by the elastic processes and also by the Newtonian attraction of the surrounding masses which leads to mean values close to the elastic limit of -0.23 μGal/mm.
This study focused on the hydrological loading. However, many other elastic loading processes (due to oceans, atmosphere, ice) are present in gravity and vertical displacement measurements. Because of their different spectral content, the gravity/height ratio will be different from those presented here. Moreover values found in this study may be different from those deduced from field measurements because of the bad modeling of the very local effects not taken into account in the global loading models.

References

Farrell W.E., 1972. Deformation of the earth by surface loads, *Rev. Geophys. Space Phys*., **10**, 761-797.
Merriam J.B., 1980. The series computation of the gravitational perturbation due to an ocean tide, *Phys. Earth Planet. Int.*, **23**, 81-86.
Milly P.C.D. & A.B. Shmakin, 2002. Global modeling of Land Water and Energy Balances. Part I: The Land Dynamics (LaD) Model. *J. Hydrometeor.,* **3**, 283-299.
Spratt R.S., 1982. Modelling the effect of atmospheric pressure variations on gravity, *Geophys. J. R. Astr. Soc*.,**71**, 173-186
Wahr J., H. DaZhong & A. Trupin, 1995. Predictions of vertical uplift caused by changing polar ice volumes on a viscoelastic earth, *Geophys. Res. Lett.*, **22**, 977-980.

Gravity variations and displacements caused by storm surge loading on the north-west European shelf.

T. F. Baker [1], F. Fratepietro [1], S. D. P. Williams [1] and M. Van Camp [2]
[1]Proudman Oceanographic Laboratory, Joseph Proudman Building, 6 Brownlow Street, Liverpool, L3 5DA, UK.
[2]Observatoire Royal de Belgique, 3 Avenue Circulaire, B-1180 Bruxelles, Belgium.

Superconducting gravity, absolute gravity and space geodetic measurements have to be corrected for various surface loading signals in order to obtain improved time series of long term crustal deformations due to tectonic or glacial isostatic adjustment (e.g in the UK, a network of continuous GPS stations and a smaller number of absolute gravity stations have been set up in order to monitor vertical land movements due to post-glacial rebound/subsidence and to provide corrections for vertical crustal movements at tide gauges; see Teferle et al., 2006).

These loading corrections are usually made by using global loading models e.g. atmospheric pressure, hydrological, tidal and non-tidal loading models. In the work described here we concentrate on the corrections for non-tidal ocean mass variations. Most of the global non-tidal ocean loading models that have been used for correcting geodetic measurements have a fairly low resolution e.g. 1 x 1 degrees and these are not able to adequately resolve the large mass variations on shallow continental shelves. In the present work, we compute the non-tidal ocean loading deformations caused by storm surges on the north-west European shelf using the output from a 12 km grid storm surge model. The spatial distributions of the vertical and horizontal displacements and the gravity variations caused by a typical storm surge event are computed in order to show the magnitudes of the effects that can be expected in space geodetic or gravity measurements. A storm surge of just over 2 m in the southern North Sea produces vertical displacements of -20 to -30 mm and increases of gravity of 6 to 8 μgal in the coastal areas of Denmark, Germany, the Netherlands and the east coast of England. It is shown that the loading deformations due to surges affect a wide area of north-west Europe. Although the GGP station at Membach, in Belgium, is about 200 km from the North Sea, there is evidence for storm surge loading in the gravity data. This type of high resolution non-tidal loading model is required for correcting geodetic measurements made in all areas of the world near shallow continental shelves.

A paper has recently been published in Geophysical Research Letters, which gives further information on this work (Fratepietro et al., 2006).

REFERENCES

Fratepietro, F., T. F. Baker, S. D. P. Williams and M. Van Camp (2006), Ocean loading deformations caused by storm surges on the northwest European shelf, Geophys. Res. Lett., *33*, L06317, doi:10.1029/2005GL025475.

Teferle, F. N., R. M. Bingley, S. D. P. Williams, T. F. Baker and A. H. Dodson (2006), Using continuous GPS and absolute gravity to separate vertical land movements and changes in sea-level at tide-gauges in the UK, Phil. Trans. Roy. Soc. A, *364*, 917-930, doi:10.10198/rsta.2006.1746.

${}_oS_o$: gravity and strain and Earth's radius

by Walter Zürn and Ruedi Widmer-Schnidrig
Black Forest Observatory, Universities Karlsruhe/Stuttgart, Heubach 206,
D-77709 Wolfach, Germany

The N-Sumatra - Andaman Islands earthquake on December 26, 2004 with a moment magnitude between 9.0 and 9.3 excited the free oscillations of the earth to amplitudes such that due to the improvements of instrumentation during the last 40 years measurements with unprecedented quality could be obtained. Specifically the "breathing mode" ${}_oS_o$ could be observed on vertical accelerometer records in the time domain for several months. On March 28 the second Sumatra event (8.7) reexcited this mode. We determine the frequency and Q of the mode with higher precision than before from a single data set from the STS-1/Z broadband seismometer at BFO. The initial radial amplitude was about 1/20 mm. This mode was also clearly observed on the 10-m Invar wire-strainmeters at BFO with an amplitude of about $8 \cdot 10^{-12}$. The radial and strain amplitudes are geometrically related involving the radius of the Earth. We carry out a consistency check between the amplitudes and Earth's radius. The quality of this check is limited by the small amplitude in strain and the resulting low signal-to-noise ratio.

Effects of the Earth's asymmetry on $_0S_0$ amplitude: predictions and observations after the 2004 Sumatra-Andaman earthquake

Severine Rosat, Shingo Watada and Tadahiro Sato

The 2004 Sumatra-Andaman earthquake with a moment magnitude greater than 9 has strongly excited the low-frequency seismic modes, particularly the seismic mode $_0S_0$. $_0S_0$ is a radial fundamental spheroidal mode called "breathing mode" of the Earth that oscillates at a period of 20.5 minutes and that is associated with changes in the Earth's circumference. Amplitude measurements of $_0S_0$ at 11 Superconducting Gravimeters (SGs) sites reveal a clear latitude dependency of ± 2% in deviation from the mean amplitude between the latitudes 80°N and 40°S. In a non-rotating spherically symmetric Earth's model (PREM-like model), $_0S_0$ amplitude is the same all over the Earth's surface. The Earth's rotation and ellipticity introduce a strong coupling of $_0S_0$ with the spheroidal harmonic degree two $_1S_2$, $_0S_2$ and $_2S_2$ modes through elliptic figure of the Earth and with the toroidal degree one $_1T_1$ and $_2T_1$ modes through the Coriolis force. The coupling effect through the rotation and ellipticity perturbs $_0S_0$ amplitude by introducing a latitude dependency with a maximum change of 1% between the equator and the pole. When we introduce the seismic lateral heterogeneities, $_0S_0$ strongly couples to $_0S_5$, and next to $_1S_2$. $_1S_3$, $_4S_2$, $_3S_2$ and $_0S_2$ also couple to $_0S_0$. In this case we observe both a latitude and longitude dependency of $_0S_0$ amplitude at the Earth's surface and $_0S_0$ amplitude is 2% higher at the pole than at the equator. The variation of $_0S_0$ amplitude as a function of latitude is therefore consistent between the theoretical predictions and the observations.

Combined gravimetric and VLBI free core nutation parameter Bayesian inversion

FLORSCH Nicolas[(1)], LLUBES Muriel[(2)], PETROV Leonid[(3)], BOY Jean-Paul[(4)], HINDERER Jacques[(4)]

[(1)]UMR 7619 – CNRS/UPMC - Case 105, 4 place Jussieu, 75252 Paris Cedex 05, France
[(2)]UMR 5566 – CNRS/OMP – 14 av. Edouard Belin, 31400 Toulouse, France
[(3)]National Astronomical Observatory, Mizusawa, 2-12, Hoshigaoka-chyo, Mizusawa, Iwate, 023-0861, Japan
[(4)]UMR 7516 – CNRS/ULP – 5 rue Descartes, 67084 Strasbourg cedex, France.

The fluid core resonance phenomenon affects the amplitude of the tidal waves close to the diurnal period. Although this has been studied for a long time, the accuracy of most relevant resonance parameters (resonance frequency and quality factor) improves rather slowly. This is mainly due to the fact that ground-based experiments that can be used to retrieve these parameters (gravimeters, deformations as derived from VLBI measurements) undergo oceanic tidal loading that degrade the signal/noise ratio. We use here recent oceanic loading estimations and discuss their accuracy to correct raw gravimetric data. We also determine the most useful waves to be used in the inversion scheme by undertaking a sensitivity analysis. Then, we use a Bayesian inversion method to determine and combine superconducting gravimetric data from specific stations belonging to the Global Geodynamic Project with vertical displacement data as derived from the VLBI network (horizontal displacements having been found too noisy for that purpose). This actually permits to analyse and compare the respective informative contribution of each network, to fully quantify the level of certainty of the retrieved quantities, and finally to retrieve suitable uncertainty ranges for the FCN period and quality factor.

First Data Analysis of MunGyung Superconducting Gravimeter in Korea

Jeong Woo Kim, Juergen Neumeyer, Taehee Kim, Ik Woo, and Hyuck-Jin Park

A new Superconducting Gravimeter (SG) was installed at MunGyung (MG), Korea, where geodetic and geophysical instruments are combined for the Korean National Lab Project "Optimal Data Fusion of Geophysical and Geodetic Measurements for Geological Hazards Monitoring and Prediction." For installing the SG, a new measuring hut with the grounded pier was built. The SG has been operating since March 2005. In addition, local atmospheric pressure has been recorded and a borehole was drilled in September 2005 close to the SG site for measuring groundwater level changes. At MG site a GPS ground station is also being operated with borehole seismic accelerometer. First calibration coefficient was determined based on the theoretical tides. After pre-processing, the first tidal analysis has been performed and compared with the Wahr-Dehant model parameters. The atmospheric pressure and ground water level induced gravity variations are shown. From the gravity residuals, the drift characteristics of the SG was estimated. When analysing the gravity data, a disturbing oscillation was detected. The oscillation was spectrally analyzed and compared with the behaviour of the SG tilt levelling system to search for a reason.

Integration of the GGP ISDC in the new ISDC portal

B. Ritschel

The new GFZ ISDC portal consolidates the unique and only project related ISDC (Information System and Data Center), like GGP-ISDC, CHAMP-ISDC and GRACE-ISDC. The overall data features and applications of the ISDC portal are based on an open source Internet portal framework and additional specific software modules. This first step in the integration of geodetic and geophysical data and information management is providing the scientific community with unified services in product retrieval and data access. For the integration and harmonization of different types of geo data especially a sufficient and standardized data description using suitable metadata is necessary. Most of the GGP data related metadata are kept in different non standardized documents or database tables or stored in the header of the data files only. In order to enhance the import of GGP data into the new ISDC portal and for a real cross retrieval of GGP and other geo data the application of a metadata standard for GGP data is necessary now.

Evaluation of M4 ocean tide loading inside the GGP network

Ducarme Bernard[1], Zhou Jiangcun[2], Sun Heping[2]

[1] Research Associate NFSR, Royal Observatory of Belgium, Av. Circulaire 3, B-1180 Brussels, Belgium.

[2] Institute of Geodesy and Geophysics, Chinese Academy of Sciences, 340 Xu Dong road, 430077 Wuhan, China.

Abstract

The determination of M4 from tidal gravity records is not a trivial problem. The amplitude at the equator does not exceed 27 nanogal (1ngal=10^{-11}m.s^{-2}) and drops to 6.7 nanogal at a latitude of 45°. Quarter-diurnal (QD) spectrum has been accurately determined in the superconducting gravimeters (SG) records using the new VAV tidal analysis program. Recently the FES04 ocean tides model provided a world map for M4. The worldwide distribution of Global Geodynamics Project (GGP) stations equipped with SG's provides a good opportunity to check the capacity of this model to provide reliable tidal loading estimations. The West European area with its concentration of SG observations and several local models available for M4 is the best test area. Tidal loading on M4 frequency is still important at several hundred kilometres inside the continent. In Europe the results for M4 points clearly to a better efficiency of the tidal loading corrections computed using the Pingree & Griffiths model. The final residue reaches the level of 1ngal only for stations beyond 10° of East longitude. Reasonable tidal factors are obtained in stations (Boulder and Wuhan), where the loading is weak and the theoretical amplitude at the level of 10 ngal. It means that instrumental nonlinearities are not producing spurious signals at M4 frequency. Generally however the M4 tide included in the ocean model FES04 does not provide efficient tidal loading corrections for tidal gravity observations.

Keywords: non-linear tides, superconducting gravimeter, GGP

1. Intoduction

Quarter-diurnal (QD) spectrum has been clearly identified in the superconducting gravimeters (SG) records since a long time (Florsch et al., 1995). The main QD non linear tides due to ocean tides loading are present in the stacking of SG data used for the identification of the Slichter's modes (Sun et al., 2003, 2004). It should thus be important to be able to suppress these non-linear tides from the residues at the level of the tidal analysis. It is now possible using the VAV tidal analysis software (Venedikov et al., 2003, 2005; Ducarme et al., 2006).

The recent FES04 ocean tides model (/pub/soa/mare/tide_model/ global_solution/fes2004/tide/ at ftp.legos.obs-mip.fr) is providing a global map for the quarter-diurnal wave M4, which is the main QD non-linear tidal constituent. Its amplitude can be large on the continental shelf, typically along the European coast from the Gulf of Biscay to the North Sea or on the Patagonian shelf. The worldwide distribution of GGP stations (Fig. 1-3, Crossley et al., 1999, http://www.eas.slu.edu/GGP/ggpmaps.html,), equipped with superconducting

gravimeters (SG), is a good opportunity to check the capacity of this model to provide reliable tidal loading estimations. The West European area with its concentration of SG observations and several local models available for M4 is the best test area. However the determination of M4 from tidal gravity records is not a trivial problem. The amplitude at the equator does not exceed 27 nanogal ($1ngal=10^{-11}m.s^{-2}$) and drops to 6.7 nanogal at a latitude of 45°. Moreover several non linear tides, which are not existing in the tidal potential, are generated in the shallow waters: "shallow water tides" (SWT) (Boy et al., 2004).
As M2 is one of the main tidal constituents in the astronomical tides, any non-linearity in the sensor and its electronics will produce a spurious M4 wave mixing up with the true tidal gravity wave and the indirect effect of the ocean tide. Other non-linear tides can be created also in a way similar to the shallow water constituents. As all the SGs have a similar design we could have a systematic effect. It is thus important to find in the GGP network stations with very low ocean tide loading for M4 and check if the tidal parameters obtained in such places are close to the models of response of the Earth to the tidal potential of degree four.
In this paper we shall first discuss the optimisation of the determination of the M4 tide in the tidal gravity records and then compare our results with several ocean tides models in Europe and with FES04 alone in the rest of the world.

2. Quarter-diurnal spectrum

The spectrum of the quarter-diurnal waves coming from the potential of degree 4 order 4 is limited to a few main constituents (Table 1, Tamura, 1987).

Table 1: Main tidal components from the W_4^4 potential according to Tamura, 1987
Amplitudes are given in nanogal ($10^{-11}m.s^{-2}$)

Wave	Angular speed °/h	Doodson number	Amplitude at φ=45°
N4	56.87945907	435.755	0.52
3MS4	56.95231272	437.555	0.46
MN4	57.42383377	445.655	2.40
2MLS4	57.49668743	447.455	0.46
M4	57.96820848	455.555	6.69
ML4	58.51258319	465.455	0.28
KN4	58.52186681	465.655	0.57
MK4	59.06624152	475.555	1.18

The amplitudes are four times bigger at the equator as the dependence is in $\cos^4\varphi$.
Besides M4 one will notice its two elliptic waves MN4 and ML4. The groups can be separated on one month, except for (N4,3MS4) and (MN4,2MLS4). For these groups 6 months are required. ML4 and KN4 form a single group that can be separated on 4 years, as their arguments differ only by two times the lunar perigee argument.
It should be noted that, with long SG records, the RMS error is at the level of 0.2ngal ($210^{-12}ms^{-2}$) in amplitude, in the best signal to noise conditions, and is

generally close to 0.4ngal. In such conditions it is very difficult to determine precise tidal factors for waves below 1nms^{-2} and one should limit the tidal separation to the three main constituents MN4 (group 435-447), M4 (group 455) and MK4 (group 465-475).
On the other hand, 18 non-linear tides (SWT) identified in the GGP SG records, are listed in table 2. These terms do not always coincide with waves identified in the tidal potential.
It should be noted that the main wave M4 is surrounded by the semi-annual modulations $\pm|S2\text{-}K2|$, corresponding to an annual amplitude modulation of the constitutive semi-diurnal terms. For example 2MSK4 is equivalent to α_4 and 2MKS4 to β_4. These last waves have not been observed with SG, except in Sutherland.

Table 2: non-linear tides (shallow water components) observed in the SG records

Wave	generation	Angular speed °/h
2MNS4	2*M2+N2-S2	56.40793843
•N4	N2*N2	56.87945907
2Mν S4	2*M2+ν2-S2	56.48079200
N4	2*N2	56.87945906
•3MS4	3*M2-S2	56.95231272
MSNK4	M2+S2+N2-K2	57.34169649
•MN4	M2+N2	57.42383377
Mν4	M2+ν2	57.49668743
2MSK4	2*M2+(S2-K2)	57.88607120
•M4	2*M2	57.96820848
2MKS4	2*M2+(K2-S2)	58.05034576
SN4	S2+N2	58.43972953
•KN4	K2+N2	58.52186681
MT4	M2+T2	58.94303756
MS4	M2+S2	58.98410424
•MK4	M2+K2	59.06624152
SL4	S2+L2	59.52847895
*S4	S2*S2	60.00000000
SK4	S2+K2	60.08213278

* from meteorological origin
• already present in the tidal potential

From these considerations we can derive three possible ways for the determination of M4 in tidal records:
- Separate the three main tidal groups MN4, M4 and MK4, without introduction of additional non linear tides;
- Introduce non linear tides only (shallow only solution);

- Put all tidal waves coming from the potential in one single M4 group and introduce selected additional non linear tides. These terms will take into account the difference between the tidal factor at each perturbed frequency and the tidal factors of M4.

The VAV tidal analysis method provides an easy way to select the optimal solution through the "Akaike Criterion" (AIC, Sakamoto et al., 1986). For different computations using the same data set and different unknowns the best solution corresponds to a minimum value of AIC.

The use of AIC coupled with a 3σ signification test allows also the selection of the SWT really present in any tidal record. As example we show below two correction steps at Sutherland. In Figure 1 the spectrum of the original data is compared with the tidal potential, showing a large SWT (MS4), not existing in the Tamura potential, as well as the meteorological wave S4. In figure 2 the major components have been eliminated (AIC=6231). A few spectral peaks are still visible i.e. from left to right two side waves of MN4, MT4 and several side lobes of S4. These last spectral peaks correspond to the annual and semi-annual modulations of the meteorological wave S4.After elimination of 11 components significant at the 3σ level and of the meteorological waves the final spectrum is nearly flat (AIC=5948). A similar approach is possible in any tidal band. It is thus possible to clean individually all the GGP stations records before the application of sophisticated detection methods for the detection of the Slichter modes or any core mode.

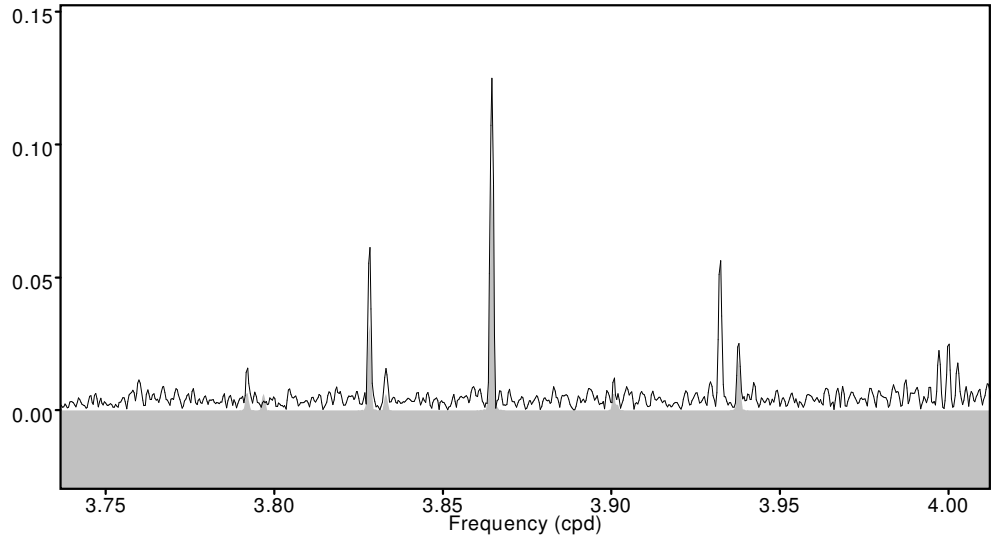

Figure 1: Spectrum at Sutherland: residues (full line) and tidal potential (shaded)

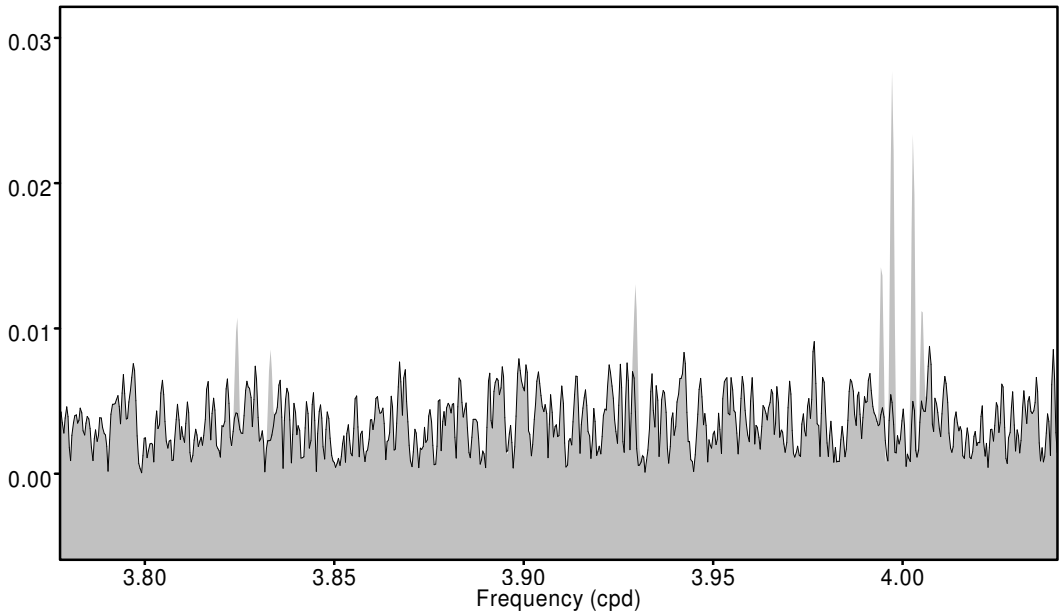

Figure 2: improved gravity residues at Sutherland : first elimination step (shaded) and final (full line)

3. Detection of the quarter-diurnal tides by the GGP network (Table 3)

The "shallow only" solution does never correspond to the optimal one, except when the amplitude of the astronomical tide is very weak as in Ny Alesund (NY) and Syowa (SY). In these stations all the observed QD tides are purely non-linear ones. The solution with the tidal potential alone was optimal in two stations only (BO and WU), where only one shallow water tide is significant (Table 3). A maximum of 11 significant non linear terms, including α_4 and β_4 was found in Sutherland (SU) (Figure 1). The pure non-linear tides terms MS4 and SK4 are observed in 15 stations among 21. In Europe a maximum of 10 non linear tides are observed in Moxa (MO). The number of observed terms depends in a critical way from the signal to noise ratio, which is very high in MO, and from the distance to the sea. We observe only 4 terms in Vienna (VI) (Figure 2), where the data quality is the same. A higher number of non linear terms are observed in Medicina (MC), probably due to the vicinity of the Adriatic Sea.

A general conclusion is that quarter-diurnal non linear terms are present in gravity records even far from the coast. It is a reason why they were found in the stacking of tidal gravity records used for the detection of the Slichter modes (Sun et al., 2003, 2004).

Table 3: Quarter-diurnal tides detected by the GGP network
N: number of observed non-linear tides
Theoretical (A_{th}) and observed (A_o) amplitudes are in ngal ($10^{-11}nms^{-2}$)
MSD: mean square deviation of the unit weight in ngal ($10^{-11}nms^{-2}$)
Stations are listed by order of increasing M4 amplitude from poles to equator

Station		M4*		MN4*	MS4	MK4*	SK4	N	MSD
		A_{th}	A_o	A_o	A_o	A_o	A_o		
Ny Alesund	NY	0.04	24.89±1.46	10.16	9.20	5.20	2.33	6	180
Syowa	SY	0.44	29.86±0.88	14.92	12.07	3.30	4.13	10	96
Metsahovi	ME	1.63	0.29±0.36	-	1.08	0.81	-	3	68
Potsdam	PO	3.72	1.57±0.44	1.04	1.42	-	1.63	3	66
Brussels	BE	4.28	4.09±0.55	2.44	3.67	1.45	-	4	136
Moxa	MO	4.33	1.25±0.20	1.10	1.00	0.89	1.12	10	40
Membach	MB	4.35	2.08±0.26	2.08	2.02	0.81	-	4	52
Bad Homburg	BA	4.49	1.42±0.28	2.47	1.80	1.27	1.17	6	53
Wettzell	WE	4.91	1.63±0.20	1.51	1.59	0.41	1.35	5	45
Strasbourg	ST	5.12	2.34±0.23	2.64	2.81	1.08	0.89	7	41
Vienna	VI	5.27	2.51±0.23	0.87	1.17	0.89	0.73	4	39
Cantley	CA	6.43	4.98±0.36	1.45	1.05	1.05	0.74	6	73
Medicina	MC	6.93	2.73±0.27	1.84	3.55	1.10	1.33	8	46
Boulder	BO	9.16	10.24±0.41	1.54	-	-	-	1	67
Esashi	ES	9.69	11.91±1.44	8.13	3.49	2.80	3.45	4	203
Tigo/Concepc.	TC	10.99	15.59±0.72	8.27	2.18	2.53	1.22	6	73
Matsushiro	MA	11.17	10.59±0.45	2.34	1.55	-	2.19	4	66
Canberra	CB	11.88	17.37±0.29	1.42	4.25	0.82	1.63	7	52
Sutherland	SU	13.63	33.87±0.34	6.60	8.85	3.81	0.99	11	60
Wuhan	WU	14.76	15.54±0.41	-	-	1.07	-	1	61
Bandung	BA	26.00	21.64±0.94	4.53	14.01	3.91	-	6	93

* quarter-diurnal wave present in the tidal potential

4. Updated results for M4 in Europe

The different tidal vectors (**A**, **R**, **L**, **B**, **X**), used below, are described in Figure 3.
In a recent paper Boy et al. (2004) tried to model the ocean tides loading in West Europe for the tidal wave M4 using different ocean tides models (Mog2D, Pingree and Griffiths, 1980 and Flather, 1976), covering the English channel, the gulf of Biscay, the North sea, the Irish sea and the North Atlantic. The authors compare directly the "observed non-linear tidal loading" (OTL) vector obtained in 8 European GGP stations (Table 2 in Boy et al., 2004) with the computed ocean load vector $\mathbf{L}(L,\lambda)$ (Table 5 in Boy et al., 2004). The phase of the load vector with respect to Greenwich is quite homogeneous from Strasbourg to Vienna (Table 4). The behaviour of the station Metsahovi (ME) is different and it is not surprising as it is geographically separated from the other European stations and close to the Gulf of Finland. The most recent model Mog2D is giving load vector amplitudes

which are twice as large as the OTL vectors (**B** in Table 5), while Pingree & Griffith model is closer to the observations. The phase agreement of these two models with the observations is very good for inland stations (Brussels, Membach and Metsahovi) excluded, while Flather's model displays a strong phase bias. This last model is not displayed in Table 4.

Table 4: Tidal loading computation for M4 in Europe
Amplitudes are given in ngal (10^{-11}nms^{-2})
Greenwich phase in degrees and oceanographic convention

Station	Residue **B**		FES04 **L**		Pingree&Griffiths **L***		Mog2D **L***	
	B	β	L	λ	L	λ	L	λ
	RMS							
BE	4.65	215.8	3.5	121.2	4.0	266.8	8.8	94.4
Brussels	*±.55*	*±7.7*						
MB	3.88	183.2	3.4	151.7	4.3	217.8	9.0	122.0
Membach	*±.26*	*±7.3*						
ST	7.64	147.9	5.5	180.6	4.9	158.9	11.4	141.4
Strasbourg	*±.23*	*±5.7*						
MO	3.61	146.1	3.9	176.9	3.4	147.6	7.3	142.9
Moxa	*±.20*	*±9.0*						
WE	4.56	146.8	3.4	178.9	3.4	152.8	7.0	142.8
Wettzell	*±.20*	*±7.1*						
PO	2.31	131.4	3.1	169.1	3.1	138.3	6.6	147.0
Potsdam	*±.44*	*±16.1*						
VI	3.54	135.4	2.5	181.6	2.9	152.2	5.5	142.8
Vienna	*±.23*	*±5.2*						
ME	1.96	78.7	3.1	130.2	2.7	137.0	3.5	163.3
Metsahovi	*±.36*	*±7.0*						

* taken from Table 5 in Boy et al.., 2004

In this study we compute first the tidal loading vector **L** at the same sites using the FES04 model (Table 4, Figure 4). The tidal loading vector **L**, which takes into account the direct attraction of the water masses, the flexion of the ground and the associated change of potential, was evaluated by performing a convolution integral between the ocean tide models and the load Green's function computed by Farrell (Farrell, 1972). To compute the residual vector **B**(B,β) we subtracted from the observed amplitude vector **A**(A,α), the body tide response **R**(δ_{th} A_{th},0), using a theoretical amplitude factor δ_{th}= 1.038 corresponding to the W_4^4 tidal potential (Dehant et al., 1999). The theoretical amplitude is given for each station in Table 5. This **B** vector should be compared with the OTL vector in Boy et al., 2004. However we used longer time series than these authors.
There is a systematic phase difference of the order of 30° to 40° between the load computations using Mog2D and FES04. The amplitude L computed by Mog2D is

twice the amplitude deduced from FES04, which in turn is close to Pingree & Griffiths.

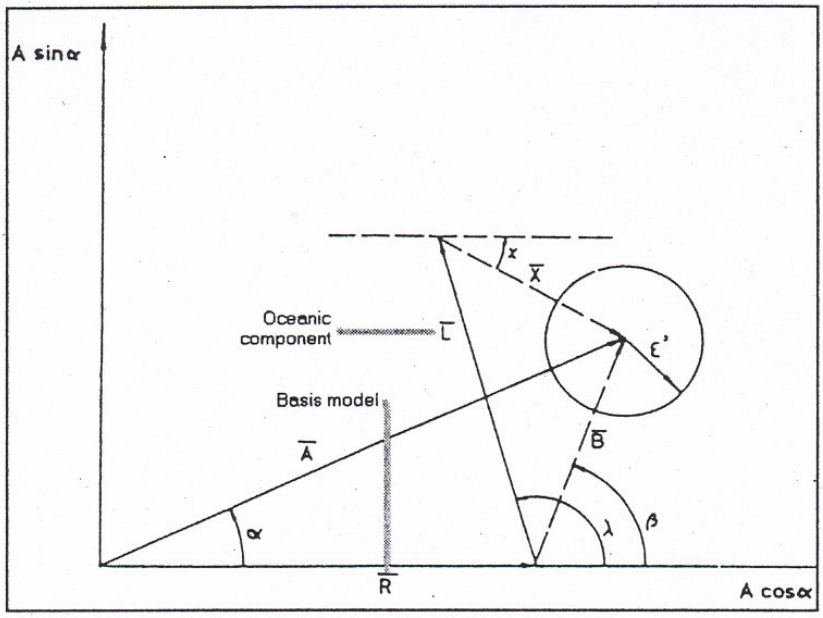

Figure 3: Relationship between the observed tidal amplitude vector **A**(A,α), the Earth model **R**(R,0), the computed ocean tides load vector **L**(L,λ), the tidal residue **B**(B,β) = **A** – **R** and the corrected residue **X**(X,χ) = **B** - **L** .

The residual vector (Table 4, Figure 4) agrees within the RMS errors with the OTL vector given in the table 2 of Boy et al, 2004. It shows that the results of the data analysis are very stable. Obviously Pingree & Griffiths model is the only one able to recover the strong phase decrease between BE and ST and the amplitude of the load vectors is always close to the observed residue **B**. FES04 is predicting correctly the amplitudes but its phases are always too large from Strasbourg (ST) to Vienna (VI). On the contrary, the phases of Mog2D are generally in good agreement with the observations, while the amplitudes are much too large.
Table 5 displays the final residue

$$\mathbf{X}(X,\chi) = \mathbf{B}(B,\beta) - \mathbf{L}(L,\lambda),$$

which represents the unexplained part of the residual vector after correction using the Pingree & Griffiths model. One notices a strong diminution for the central European stations (MO, WE, PO, VI) and a diminution by a factor of two in ST, but a slight improvement only for BE and MB. Obviously no model is able to represent correctly the tidal loading at M4 frequency for stations with longitude less than 10°.
As a conclusion, we cannot really trust the M4 ocean tide correction extracted from the FES04 model in Europe, due probably to a still too coarse grid.

Table 5: Tidal residues for M4 in Europe corrected with Pingree & Griffiths map
A_{th}: theoretical amplitude for M4, σ: RMS error
Amplitudes are given in ngal (10^{-11}nms^{-2})
Greenwich phase in degrees and oceanographic convention

Station	Residue **B**		Final Residue **X**		A_{th}	Pingree & Griffiths **L***	
	B	β	X	χ		L	λ
	σ	σ					
BE	4.65	215.8	3.76	160.3	4.3	4.0	266.8
Brussels	*±.55*	*±7.7*					
MB	3.88	183.2	2.45	101.7	4.4	4.3	217.8
Membach	*±.26*	*±7.3*					
ST	7.64	147.9	3.00	180.6	5.1	4.9	158.9
Strasbourg	*±.23*	*±5.7*					
MO	3.61	146.1	0.28	127.3	4.3	3.4	147.6
Moxa	*±.20*	*±9.0*					
WE	4.56	146.8	1.22	129.7	4.9	3.4	152.8
Wettzell	*±.20*	*±7.1*					
PO	2.31	131.4	0.83	-22.1	3.7	3.1	138.3
Potsdam	*±.44*	*±16.1*					
VI	3.54	135.4	1.14	88.8	5.3	2.9	152.2
Vienna	*±.23*	*±5.2*					
ME	1.96	78.7	2.39	1.4	1.6	2.7	137.0
Metsahovi	*±.36*	*±7.0*					

* taken from Table 5 in Boy et al.., 2004

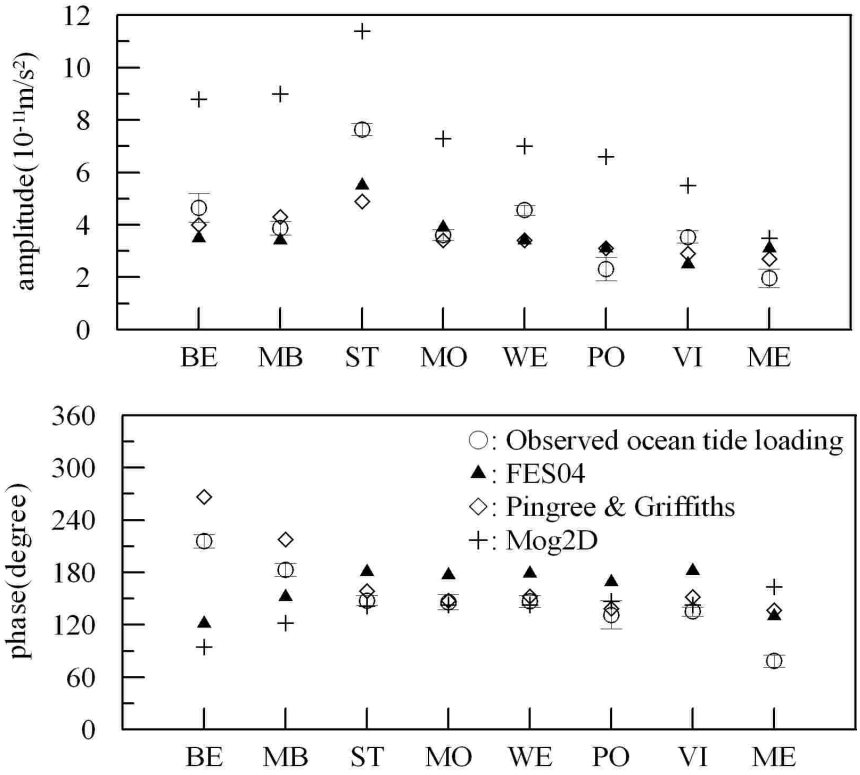

Figure 4: Observed residue (**B**) and computed (**L**) ocean tide loading vectors for three different models

5. Results for the rest of the world

We are mainly interested by two different situations:

- stations with a weak loading where we can directly observe the body tides if the theoretical amplitude is not too weak;
- stations with a large tidal loading where we can test the efficiency of the tidal loading corrections, especially when the body tides are weak.

Table 6: Tidal factors at Boulder (BO) and Wuhan (WU)
L is the amplitude of the tidal loading vector and σ the RMS error

Station	A_{th}	Observed		Corrected		L
	ngal	δ_o	α_o (°)	δ_c	α_c (°)	ngal
		σ	σ			
Boulder (BO)	9.2	1.1147	-0.954	1.1063	0.086	0.2
		±.0447	*±2.297*			
Wuhan (WU)	14.8	1.0519	-1.648	1.0984	-3.748	0.9
		±.0275	*±1.496*			

In the first category we can only select BO and WU, where the tidal loading is smaller than one nanogal and the astronomical amplitude reaches 10 ngal.

Here we introduce explicitly the observed (δ_o) and corrected (δ_c) amplitude factors. The corrected vector $\mathbf{A_c}(\delta_c A_{th}, \alpha_c)$ is given as

$$\mathbf{A_c} = \mathbf{A_o}(\delta_o A_{th}, \alpha) - \mathbf{L}(L, \lambda)$$

The results are quite good as seen from Table 6. The corrected amplitude factor is a bit too large with respect to the theoretical value δ_{th}= 1.038, but the discrepancy is still within the two sigma range. The phase differences do not differ significantly from zero. In WU the observed factor is closer to the theoretical value than the corrected one, while the tidal loading is negligible in BO. Obviously, the tidal loading correction computed from the FES04 map does not improve the results. In any case instrumental nonlinearities are not producing spurious signals at M4 frequency.

Table 7: Tidal residues for M4 corrected with FES04
A_{th}: theoretical amplitude for M4, σ: RMS error
MSD: mean square deviation of the unit weight from VAV
Amplitudes are given in ngal (10^{-11}nms^{-2})
Greenwich phase in degrees and oceanographic convention

Station	Residue		Final Residue		A_{th}	FES04	
name	B	β	X	χ		L	λ
MSD	*σ*	*σ*					
Cantley (CA)	3.0	80	1.9	73	6.4	1.1	91
60	*±.4*	*±4*					
Esashi (ES)	9.2	51	7.6	49	9.7	1.6	61
203	*±1.4*	*±7*					
Tigo (TC)	12.4	-165.0	15.5	-142	11.0	6.4	88
73	*±.7*	*±3*					
Matsushiro (MA)	8.4	48	4.2	53	11.2	4.2	44
66	*±.5*	*±2*					
Canberra (CB)	7.5	64	7.6	11	11.9	6.7	129
52	*±.3*	*±1*					
Sutherland (SU)	19.9	-98	14.3	-131	13.7	11.1	-53
60	*±.3*	*±1*					
Bandung (BA)	16.5	163	12.4	151	26.0	5.1	194
93	*±.9*	*±2*					

Among the stations with a large tidal loading we should reject coastal stations as the grid of FES04 is not fine enough. It is the case for NY and SY.

In most of the stations of Table 7, the correction does not reduce the observed residue. However the residual vector is divided by a factor of two if in Cantley (CA) and Matsushiro (MA). In Esashi (ES) the phases λ (load vector) and β (residual vector) agree but the amplitude L of the tidal loading vector is too weak. The phase of the load should be reduced of 30° in Bandung (BA) and Sutherland (SU). We have seen that the phase had to be reduced of 30° in Europe also to fit the observations. For Canberra (CB) and Tigo/Concepcion (TC) there is nothing in common between the **B** and **L** vectors.
To summarize we can say that the FES04 model seems to fit partly the observations in Eastern Canada (CA) and in Japan (ES and MA). In the Indian Ocean (SU and BA) the phase should be reduced by 30°. Moreover the amplitude is always too small to fit the observations. There is no agreement in Chile (TC) and Australia (CB).

6. Conclusions

Tidal loading on M4 frequency is still important at several hundred kilometres inside the continents. The only station without noticeable effect is Boulder (BO). Among 14 constituents listed as non-linear tides by oceanographers we can detect up to 11 constituents in some tidal gravity stations. A few of them only are present in the tidal potential at a level larger than 2ngal at the equator. M4 itself reaches only 27ngal at the equator.
The tidal gravity observations can help to discriminate between different ocean tides models if the distance to the sea is large enough to reduce the influence of the finite grid, which is not able to follow exactly the coast. In Europe the results for M4 points clearly to a better efficiency of the tidal loading corrections computed using the Pingree & Griffiths model. For stations beyond 10° of East longitude, the final residue reaches the level of 1ngal ($10^{-11}ms^{-2}$) only.
Reasonable tidal factors are obtained in stations (Boulder and Wuhan), where the loading is weak and the theoretical amplitude at the level of 10 ngal. It means that instrumental nonlinearities are not producing spurious signals at M4 frequency.
The M4 tide included in the ocean model FES04 does not provide efficient tidal loading corrections for tidal gravity observations. In Europe, where the shallow water tides are well constrained, the amplitude of the load vector is correct, but there is a 30° phase advance with respect to the observed tidal residues. A similar phase advance seems to exist in the Indian Ocean and the computed amplitude is too low. In Japan and Western Canada the phase is correct but the amplitude is too low. The model is not diminishing the observed residue in Australia (CB) and South America (TC). It is obvious that more detailed local models are required to reach a reasonable agreement between the observations and the modelled ocean tides effect. Western Europe is a good example of such agreement.
The elimination of QD components, including the non-linear tides, from the tidal residues is effective using the VAV tidal analysis program.

Acknowledgements

The stay at the Royal Observatory of Belgium of Zhou JiangCun was partly supported by the Bilateral Scientific and Technical Agreements between Belgium and China (project "SG observations and Geodynamics", BL/33/C17), and Sun Heping was partly supported by the knowledge innovation project of Chinese Academy of Sciences (KZCX2-YW-133) and National Natural Sciences Foundation of China (40730316).

BIBLIOGRAPHY

Boy, J.-P., Llubes, M., Ray, R., Hinderer, J., Florsch N., Rosat, S., Lyard, F., Letellier, T. (2004). Non-linear oceanic tides observed by superconducting gravimeters in Europe. *Journal of Geodynamics, 38 (3-5), 391-405.*

Crossley, D., Hinderer, J., Casula, G., Francis, O., Hsu, H. T., Imanishi, Y., Jentzsch, G., Kääriaïnen, J., Merriam, J., Meurers, B., Neumeyer, J., Richter, B., Shibuya, K., Sato, T., Van Dam, T. (1999). Network of superconducting gravimeters benefits a number of disciplines. *EOS, 80, 11, 121/125-126.*

Dehant, V., Defraigne, P., Wahr, J. (1999). Tides for a convective Earth. *J. Geoph. Res., 104, B1, 1035-1058.*

Ducarme, B., Venedikov, A. P., Arnoso, J., Vieira, R. (2006). Analysis and prediction of ocean tides by the computer program VAV. *J. Geodynamics, 41(1-3),100-111.*

Farrell, W. E. (1972). Deformation of the Earth by surface load. *Rev. Geophys. Space Phys.,10, 761-797.*

Flather, R.A. (1976). A tidal model of the North-West European Continental shelf. *Mém. Soc. R.Oc;, Liège, 9, 141-164.*

Florsch, N., Hinderer, J., Legros, H. (1995). Identification of quarter-diurnal tidal waves in superconducting gravimeter data. *Bull. Inf. Marées Terrestres,122, 9189-9198.*

Pingree, R.D., Maddock, L. (1978). The M4 tide in the English Channel derived from a non-linear numerical model of the M2 tide. *Deep Sea Res,.25,53-63.*

Pingree, R.D., Griffiths, K. D. (1980). Currents driven by a steady uniform windstress on the shelf seas around the British Isles. *Oceanol. Acta, 3,227-235.*

Pingree, R.D., Griffiths, K. D. (1981). S2 tidal simulationon the North-West European shelf. *J. Mar. Biol. Assoc., UK 61, 609-616.*

Sakamoto, Y., Ishiguro, M., Kitagawa, G. (1986). Akaike Information Criterion statistics. *D. Reidel Publishing Company, Tokyo, 290pp.*

Sun, H.P., Xu, J.Q., Ducarme, B. (2003). Search for the translational triplet of the Earth's solid inner core by SG observations at GGP stations. *Bull .Inf. Marées Terrestres 138, 10977-10985*

Sun, H.P., Xu, J.Q., Ducarme, B. (2004). Detection of the translational oscillations of the Earth's solid inner core based on the international superconducting gravimeter observations. *Bull. Inf. Marées Terrestres,122, 9189-9198.*

Tamura, Y. (1987). An harmonic development of the tide-generating potential. *Bull. Inf. Marées Terrestres,99, 6813-6855.*

Venedikov, A. P., Arnoso, J., Vieira, R. (2003). VAV: a program for tidal data processing. *Comput. Geosci., 29, 487-502.*
Venedikov, A. P., Arnoso, J., Vieira, R. (2005). New version of the program VAV for tidal data processing. *Comput. Geosci., 31, 667-669.*

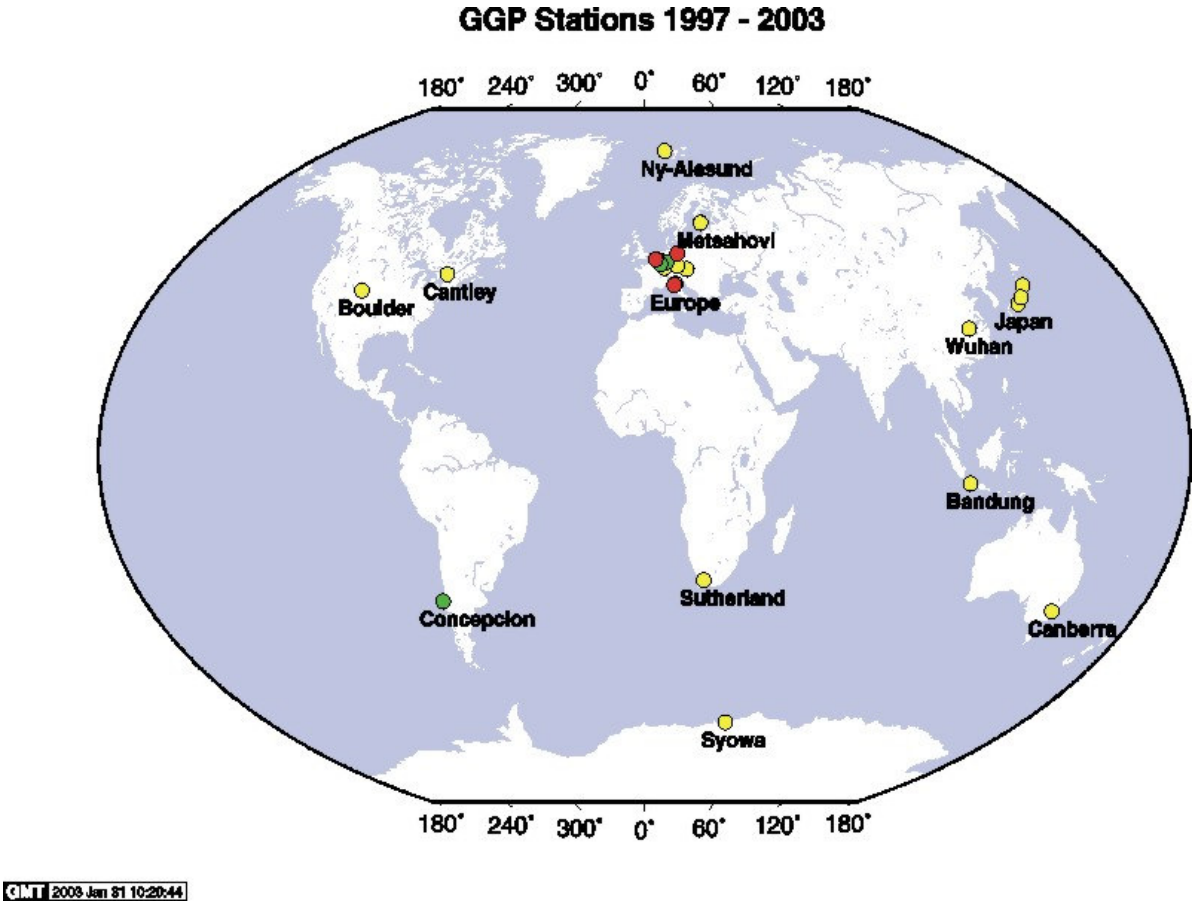

Figure 1: Global GGP network

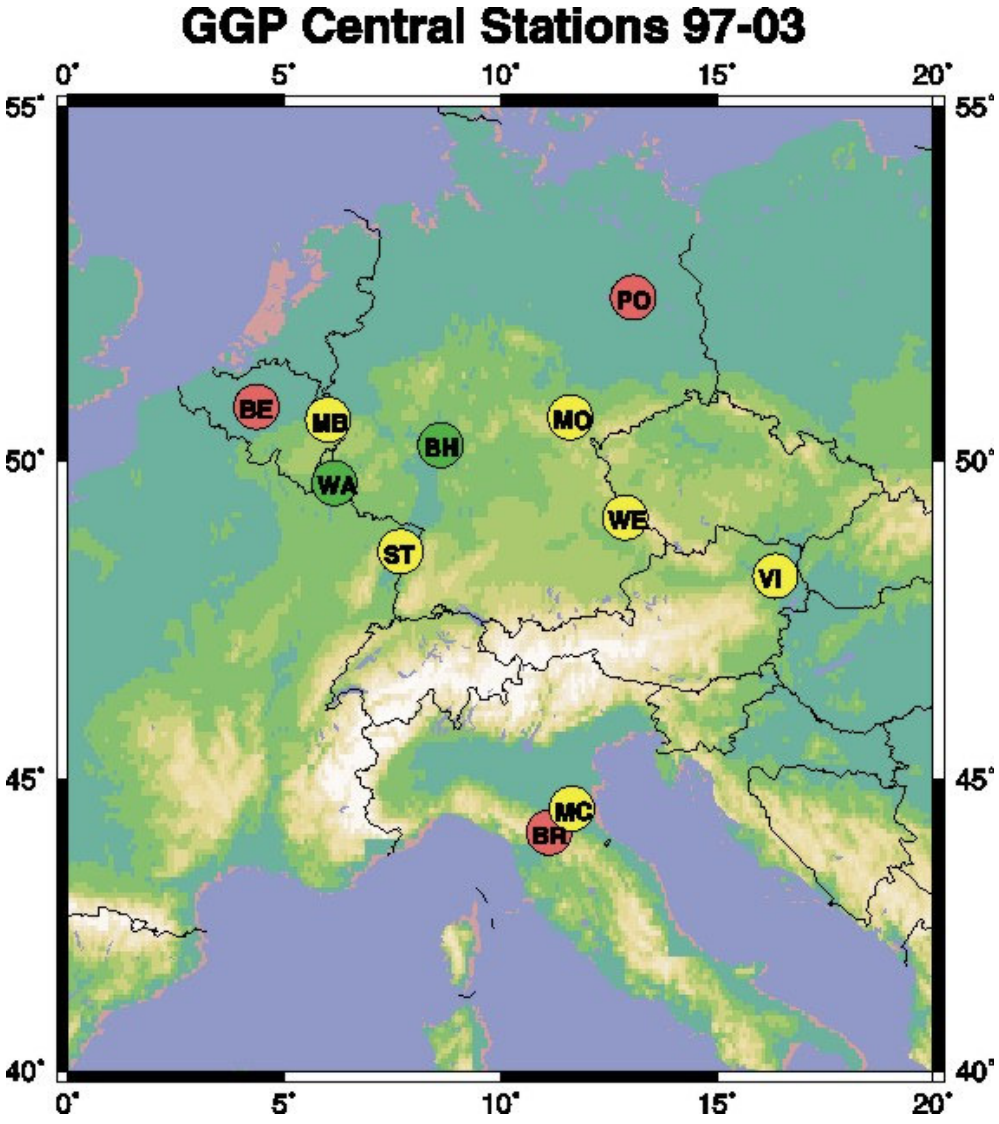

Figure 2: GGP European network

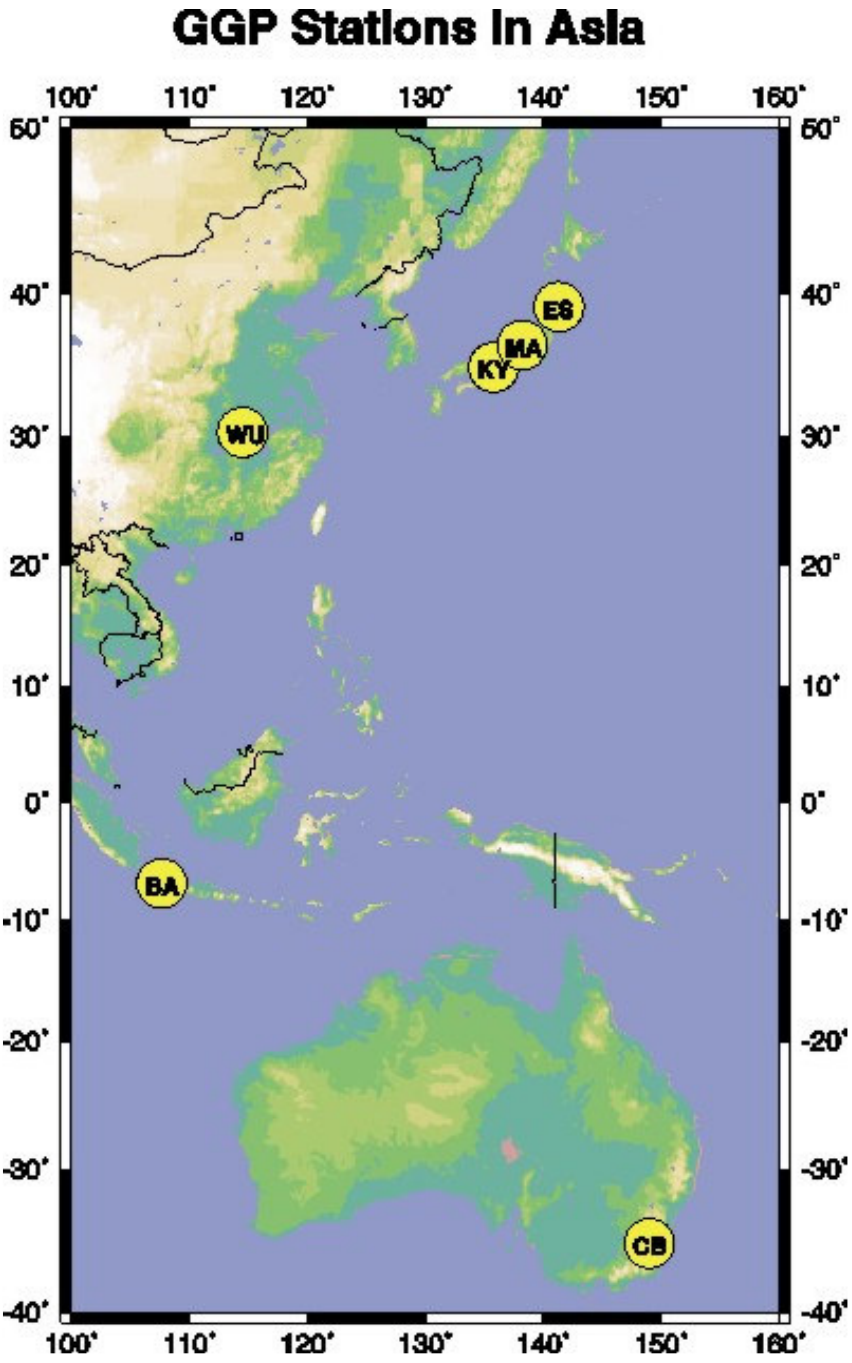

Figure 3: GGP stations in Asia and Australia

Validating the synthetic tidal gravity parameters with superconducting gravimeter observations

Zhou Jiangcun [1,2,3], Sun Heping[2], Ducarme Bernard[1]

1 Research Associate NFSR, Royal Observatory of Belgium, Av. Circulaire 3, B-1180, Brussels, Belgium

2 Institute of Geodesy and Geophysics, Chinese Academy of Sciences, Xu Dong road, 430077 Wuhan, China

3 Graduate University of Chinese Academy of Sciences, 100049 Beijing, China

Abstract Tidal gravity parameters are modeled with a Wahr-Dehant body tide model and the ocean tide models of Schw80 for M_f and CSR3.0 for 8 main diurnal and semidiurnal waves. The tidal parameters at the GGP stations are first interpolated from a 05°x05° grid. Similarly, modeled tidal parameters are computed just at the stations. From the comparison between the parameters obtained with the two approaches, it is clear that the resolution of 0.5°x0.5° is generally sufficient for interpolation. When a station is located very close to the zero-line of a tidal family the body tide model is not well constrained. When the theoretical tidal amplitude becomes very small, the tidal loading can become proportionally very large and large fluctuations of the modeled tidal factors are produced by the interpolation procedure. On the other hand, observed tidal parameters are obtained from the harmonic analysis of the superconducting gravimeters records at the GGP stations. The comparison between modeled and observed parameters shows that synthesizing tidal gravity parameters is an effective tool for tidal gravity prediction.

Keywords tidal gravity parameters, body tide model, ocean tide model, superconducting gravimeters

1 Introduction

The superconducting gravimeter, due to its high precision, high stability and low drift, ensures the accurate determination of tidal parameters including amplitude factor and phase lead. And it has a lot of applications in geodesy, geophysics and geodynamics. Due to the identical frequency content, it is impossible to separate the earth body tide from the ocean loading tide by the analysis of tidal observations. The ocean tide loading effect is computed by a convolution of the Green's function (Farrell, 1972) and ocean tide height and then subtracted from tide observations.

Previous studies showed that the ocean tide loading is the main component in the residues of the observations. Therefore, modeling tidal parameters with ocean tide loading effect and theoretical body tide derived from an Earth's model is an efficient way to get an accurate tidal prediction. Zahran compared the synthetic tidal parameters of gravity with the ones observed in Europe, and concluded that the two values are in good agreement with each other (Zahran et al, 2005).

We use the same method as Zahran's to model the tidal gravity parameters, and compare them with the results of the superconducting gravimeters inside the GGP network (Crossley et al., 1999). The stations and the data sets are listed in table 1. Due to the high precision of superconducting gravimeters, it is expected that this comparison will provide a more realistic validation of the accuracy of the synthetic tidal parameters.

Table 1: List of stations and time span of the observations

Name		latitude	longitude	height	time span
		(°)	(°)	(m)	
Ny-Alesund	NY	78.9306	11.8672	43	19990920...20041231
Brussels	BE	50.7986	4.3581	101	19820421...20000922
Membach	MB	50.6092	6.0066	250	19950804...20060403
Strasbourg	ST	48.6223	7.6840	185	19970301...20051031
Brasimone	BR	44.1235	11.1183	684	19920801...20000201
Vienna	VI	48.2493	16.3579	192	19970701...20041231
Wettzell	WE	49.1458	12.8794	612	19981104...20060630
Potsdam	PO	52.3809	13.0682	48	19920630...19981008
Moxa	MO	50.6447	11.6156	455	20000101...20060630
Metsahovi	ME	60.2172	24.3958	56	19970701...20051231
Pecny	PC	49.9170	14.7830	534	20000420...20050425
Wuhan	WU	30.5159	114.4898	89	19971220...20021127
Taiwan	TW	24.7926	120.9855	87	/
Gyungsang	GY	36.6402	128.2147	107	/
Kyoto	KY	35.0278	135.7858	60	19970701...20020731
Matsushiro	MA	36.5430	138.2070	406	19970501...20030630
Esashi	ES	39.1511	141.3318	393	19970701...20040225
Sutherland	SU	-32.3814	20.8109	1770	20001023...20050101
Bandung	BA	-6.8964	107.6317	714	19971219...20030630
Canberra	CB	-35.3206	149.0077	763	19970701...20041231
Boulder	BO	40.1308	-105.2328	1682	19950412...20031031
Cantley	CA	45.5850	-75.8071	269	19970701...20031231
TIGO	TY	-36.8470	-73.0255	100	20021205...20060630
Syowa	SY	-69.0070	39.5950	22	19970701...20030131

2 Earth's tidal gravity

Conventionally, the tide generating potential is expanded with cosine functions. For the degree 2, the tidal generating potential is represented as (Fang, 1984)

$$T_2 = \sum_p D_{i_1} K_p \cos(i_1\tau + i_2 s + i_3 h + i_4 p + i_5 N' + i_6 p_s) \quad 0 \le i_1 \le 2 \tag{1}$$

where p represents different constituents, i_1 is the order of the constituents, i.e. 0 for long period tide (LP), 1 for diurnal tide (D) and 2 for semidiurnal tide (SD). For higher degrees of the potential, there are shorter periods third-diurnal (TD), quarter-diurnal (QD),….terms. And the bracket part is depending on time through the 6 Doodson arguments (Melchior, 1983). A main difference with the conventions of the oceanographers is that the arguments are referred to the longitude of the point of interest. K_p is the normalized amplitude coefficient of the tidal expansion. For negative amplitudes one considers usually the absolute value and adds 180° to the phase of the constituents. D_0, D_1 and D_2 are the latitude dependent geodetic coefficients of LP, D and SD tides respectively. They can be written as follows

$$\begin{Bmatrix} D_0 \\ D_1 \\ D_2 \end{Bmatrix} = D_C \begin{cases} (\frac{r}{R})^2 (\frac{1}{3} - \sin^2\phi) \\ (\frac{r}{R})^2 \sin 2\phi \\ (\frac{r}{R})^2 \cos^2\phi \end{cases} \tag{2}$$

where r is geocentric height, R the mean radius of the Earth, ϕ the latitude and D_C the Doodson constant.

In the spherical approximation, the dependence of geocentric height r on latitude vanishes. Hence Earth's tidal gravity can be computed as the derivative of potential with respect to r (positive downward), that is for LP, D and SD waves respectively:

$$G = \frac{\partial T_2}{\partial r} = D_C K_p \begin{cases} \frac{2r}{R^2} (\frac{1}{3} - \sin^2\phi) \cos(i_2 s + i_3 h + i_4 p + i_5 N' + i_6 p_s) \\ \frac{2r}{R^2} \sin 2\phi \cos(\tau + i_2 s + i_3 h + i_4 p + i_5 N' + i_6 p_s) \\ \frac{2r}{R^2} \cos^2\phi \cos(2\tau + i_2 s + i_3 h + i_4 p + i_5 N' + i_6 p_s) \end{cases} \tag{3}$$

As a consequence, the LP gravity tide changes its sign across latitude of $\pm 35.26°$ and the diurnal gravity tide changes its sign across equator.

For realistic application, an Earth tide model is usually not rigid but elastic. Therefore a factor δ_2 called amplitude factor should be applied to the gravity tide, which is (Melchior, 1983):

$$\delta_2 = 1 + h_2 - \frac{3}{2} k_2 \tag{4}$$

where h_2 and k_2 are the Love numbers for degree 2.

3 Ocean tide loading

Ocean tides due to astronomic forces changes the distribution of sea water masses, which results in variation of the Earth's gravity field by means of direct attraction. Meanwhile for the elasticity of the Earth, ocean tides also deform the Earth and then changes the gravity filed. The effect from attraction and deformation is called ocean tide loading effect. From Farrell (Farrell, 1972), this effect can be numerically calculated by convolution of ocean tides and Green's function. That is

$$\Delta g = \rho R^2 \int_0^{2\pi} \int_0^{\pi} G(\psi) H(\psi, A) \sin\psi \, d\psi \, dA \tag{5}$$

in which Δg is gravity variation due to ocean tide load, ρ density of sea water, $G(\psi)$ Green's function, which is relative to angular distance ψ between load and station of interest, and $H(\psi,A)$ ocean tidal height as a function of angular distance ψ ($0 \le \psi \le \pi$) and azimuth A ($0 \le A \le 2\pi$) of the direction from station to load.

4 Synthetic tidal parameters

The synthetic tidal parameters are obtained by adding ocean tide loading effect to the theoretical body tide from an Earth tide model (Timmen, et al, 1994; Zahran, et al, 2005). For an elastic Earth model, the phase lead is zero which respect to the local tidal potential. To get the Greenwich phase, the following equation can be used.

$$P_G = P_L + i_1 \times lon \tag{6}$$

where P_G and P_L are Greenwich and local phases respectively, i_1 has the same meaning as in eq.1 and *lon* is longitude (positive to the East) of the station of interest. Traditionally, phase lag is positive in oceanography while phase lead is positive in geophysics. Therefore, for the same location, the sign of phase should be changed. Fortunately, in the NLOADF program written by Agnew (Agnew, 1997), this problem has been taken into account, i.e positive values correspond to a phase lead. Therefore the relation of equation (6) also holds for ocean tide loading effect.

Conventionally, the harmonic analysis of gravity tide provides phase differences with respect to the local tidal potential and amplitude factor always with positive sign, independently of the sign of the corresponding tidal force. As mentioned in section 2, the parallels of $\pm 35.26°$ and 0° are zero-lines of long term and diurnal tides respectively. Therefore the gravity tides at the stations over different sides of these parallels have opposite signs. Hence in synthesizing the tidal parameters, this should be taken into account, by adding adequate phase shifts (Table 2).

Table 2 phase shift for different kinds of waves of Earth's tidal gravity

Earth tides	Latitude domain	Phase shift		
		LP	D	SD
gravity	35°16′~90°	180°	0°	0°
	0°~35°16′	0°	0°	0°
	-35°16′~0°	0°	180°	0°
	-90°~-35°16′	180°	180°	0°

For convenience, we always keep the phases of theoretical tides as 0 in the local reference frame. Therefore the phase shifts in table 2 should be subtracted from the phases of the ocean tide loading vectors.

5 Results and discussions

The theoretical values of Earth's tidal gravity factors are obtained using the program 'predict' from Eterna software (Wenzel, 1996). For gravimeter records, a priori amplitude factors for the tidal waves within one wave group are used from the WAHR-DEHANT (Dehant, 1987) elliptical, uniformly rotating oceanless Earth with inelastic mantle, liquid outer core and elastic inner core (PREM elastic Earth model with mantle dispersion from ZSCHAU and WANG 1987). Ocean tide loading is calculated with the Schw80 (Schwiderski, 1980) for M_f constituent and CSR3.0 (Eanes, 1996) for 8 main constituents (Q_1, O_1, P_1, K_1, N_2, M_2, S_2, K_2). And the integral Green's function method is adopted (Goad, 1980; Agnew, 1996; Agnew, 1997).

We calculate the synthetic tidal gravity parameters at the grid points around the GGP stations. There are four points for each station, and the spatial resolution is 0.5°. And then the tidal parameters of the stations are calculated using bilinear interpolation according to the ones of the grid points. Meanwhile, the tidal parameters are directly calculated by adding the ocean tide loading effect to theoretical body tides at those stations. The comparison between the interpolated values and calculated ones will effectively verify the adequacy of the spatial resolution.

Fig.1 gives the differences of M_f for all the stations. The differences of the "in phase" component are smaller than 0.012 except for Tigo (TI) in Chile, and the ones of the "out of phase" component are smaller than 0.02. The reason why Tigo is obviously an outlier is that this station with latitude of -36.847° locates near the zero-point.

Fig.2 gives the latitude dependence of the amplitude factor. For Tigo station, the two latitudes used for interpolation are -36.75° and -38.25°. By linear interpolation, the numerical result is between the two values. Unfortunately, the real value is quite different. The largest out of phase residue is found in Canberra (CB), where the M_f amplitude is also very small.

Fig.3 gives the differences of 4 diurnal constituents (Q_1, O_1 ,P_1, K_1) for all the stations. They are smaller than 0.01 for both in phase and out of phase parts. The differences for Esashi (ES), Taiwan (TW) and Syowa (SY) are apparently larger than the ones for the other stations. The reason is that there are some grid points locating over ocean area, for which the ocean tide loading effect may not have accurately been modeled. As a consequence, there will be much bias in interpolation comparing with the value directly calculated.

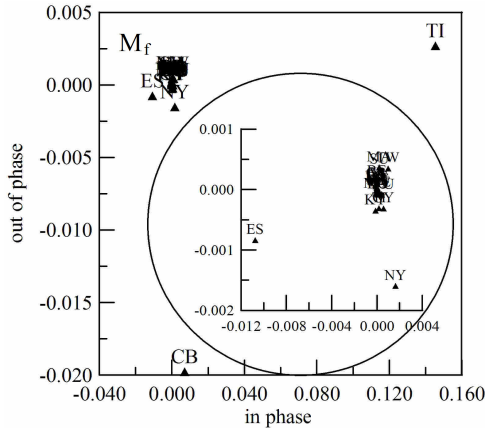

Figure 1: Differences between interpolated and calculated amplitude factors for M_f

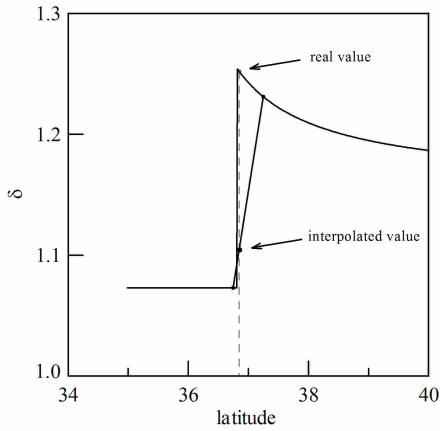

Figure 2: amplitude factor's variation as function of latitude near zero-point for long term tide

Fig.4 gives is the same as Fig3, but for the 4 main semi-diurnal constituents (N2, M2, S2, K2). As for diurnal, the differences are smaller than 0.01 for in phase and out of phase parts. Esashi (ES), Taiwan (TW) and Syowa (SY) are stations with larger differences. Additionally, the differences for Ny-Alesund (NY) station are also large due to the fact that the amplitude of the SD waves becomes very small at high latitude. For the other stations, the differences are very small.

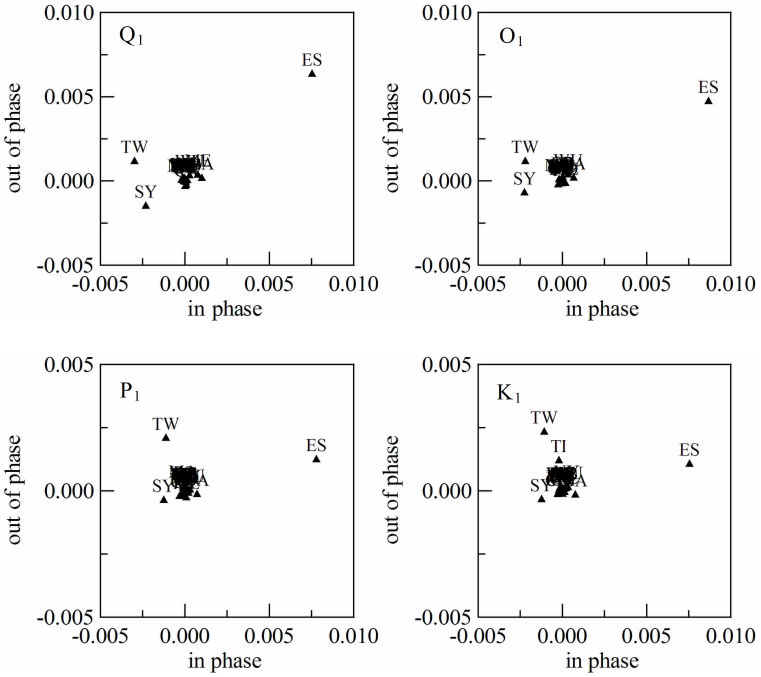

Figure 3: Differences between interpolated and calculated amplitude factors for diurnals

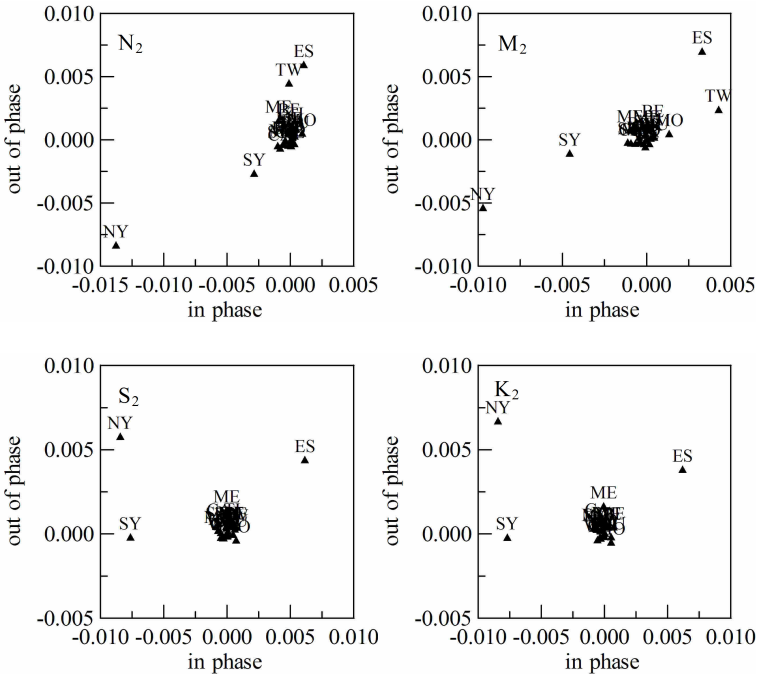

Figure 4: Differences between interpolated and calculated amplitude factors for semi-diurnals

Table 3 gives the statistical characteristics of the differences between the interpolated and directly computed values. The mean and standard deviation of the differences are computed including all the stations except for M_f for which station Tigo is excluded. The differences on the mean amplitude factors are small i.e. less than 0.0004 with standard deviation less than 0.003.

Table 3: Differences between interpolated and calculated tidal parameters for GGP stations

δ: amplitude factor, α: phase difference

	dδ		dα (°)	
wave	mean	std	mean	std
M_f	0.0003	0.0028	0.0516	0.2212
Q_1	0.0002	0.0019	0.0137	0.0625
O_1	0.0002	0.0020	0.0099	0.0463
P_1	0.0003	0.0017	0.0051	0.0245
K_1	0.0003	0.0016	0.0065	0.0258
N_2	0.0001	0.0008	0.1012	0.3991
M_2	0.0004	0.0028	0.0361	0.1098
S_2	0.0002	0.0022	0.0315	0.0964
K_2	0.0002	0.0022	0.0305	0.0968

Additionally, we compared also the tidal parameters interpolated and calculated for the 8 main waves for about 1000 stations over the world. For a better precision, only the stations of which the 4 points for interpolation around the station are all in land are adopted for the comparison. There are 638 stations satisfying this condition. Table 4 gives the statistic characteristics of the comparison. Unfortunately the result is still not yet satisfactory.

Table 4: Difference between interpolated and calculated tidal parameters for 638 stations

δ: amplitude factor, α: phase difference

	dδ		dα(°)	
wave	mean	std	mean	std
Q_1	-0.0021	0.0483	0.0623	1.3645
O_1	-0.0015	0.0443	-0.0478	3.0121
P_1	-0.0007	0.0586	0.1080	2.1945
K_1	-0.0008	0.0611	0.1067	2.2546
N_2	0.0049	0.0584	-0.0506	3.4700
M_2	0.0030	0.0578	-0.2546	3.5520
S_2	-0.0010	0.0613	-0.0988	2.2238
K_2	-0.0010	0.0604	-0.0590	2.3818

The discrepancy in table 4 is about one order of magnitude larger than in table 3. There are several reasons for that. One of the problems is that, even if many coastal stations have already been rejected when one of the 4 interpolation points is not on the land, there are still cases when one interpolation point is still close from one of the grid points of the cotidal map. Then the computed load vector is not reliable. There is a specific problem for gravity stations near equator, the zero line of diurnal tides, or at high latitude. When the ocean loading is still large, the interpolation error of the load vector produces large fluctuations of the tidal factors. We should directly compare the load vectors in stations where the theoretical amplitude of a wave is very small.

To verify the efficiency of the synthetic tidal parameters, the comparison between observed parameters and synthetic ones is carried out for the GGP stations. Table 5 gives the numerical results. As there is no observation available for stations of Taiwan/China and Gyungsang/South Korea, these two stations are excluded.

The means of the δ differences are smaller than 0.01 except for M_2. The mean phase differences are small for

diurnals while they are much larger for semi-diurnals. Because of the high latitude for Ny-Alesund station, it is difficult to determine accurate tidal parameters for semi-diurnal waves. Therefore the result excluding the station of Ny-Alesund is also given in table 5 with asterisk marked left. The differences decrease with mean dδ values close to 0.005 and mean dα values close to 0.25°. The two results are thus in reasonable agreement, given the fact that the errors on the body tides model, the error of the ocean tides model and the calibration errors (Ducarme et al., 2007, 2008) are included in the comparison.

Table 5: Difference between interpolated and observed tidal parameters at GGP station

δ: amplitude factor, α: phase difference

	dδ		dα (°)	
wave	mean	std	mean	std
Q_1	0.0017	0.0106	0.0226	0.1926
O_1	0.0022	0.0052	0.0227	0.3276
P_1	0.0030	0.0088	-0.1049	0.1313
K_1	0.0062	0.0081	-0.0334	0.1204
N_2	0.0058	0.0123	-13.9732	64.8423
M_2	0.0206	0.0735	2.8623	13.3675
S_2	0.0082	0.0208	0.4334	3.7178
K_2	0.0076	0.0225	0.6500	3.4655
$*N_2$	0.0065	0.0121	-0.1488	0.2021
$*M_2$	0.0051	0.0116	0.0127	0.2300
$*S_2$	0.0063	0.0194	-0.3588	0.1183
$*K_2$	0.0090	0.0221	-0.0866	0.2728

* Ny Alesund excluded

6 Conclusions

In the best conditions, it is possible to interpolate the tidal parameters at one station, using synthetic tidal parameters on a 0.5°x0.5° grid with a precision better than 0.003 for the amplitude factor and 0.1° for the phase, as demonstrated by the GGP stations. The synthetic tidal parameters are comparable with the observations of the superconducting gravimeters. This demonstrates that interpolation is an effective way to get the tidal gravity parameters for tidal prediction. However a general comparison involving 638 stations shows that large errors on the amplitude factors and phase differences are possible e.g. when the theoretical amplitude of the wave becomes very small. However the effect on the tidal prediction becomes then also small. For these stations the comparison should be done directly on the load vector. When the interpolation grid points are too close from the cells of the ocean tides model the computed load vector is not reliable.

Special attention should be paid to the stations located near the zero-line of a tidal family, because the interpolation may give unrealistic results for the body tides amplitude factors.

References

Agnew, D.C., 1996, SPOTL: some programs for ocean tide loading. SIO Reference series 96-8, scripts institution of oceanography, Woods Hole

Agnew, D.C., 1997, NLOADF: a program for computing ocean-tide loading, J Geophys Res, 102, 5109-5110

Crossley, D., Hinderer, J., Casula, G., Francis, O., Hsu, H. T., Imanishi, Y., Jentzsch, G., Kääriaïnen, J., Merriam, J., Meurers, B., Neumeyer, J., Richter, B., Shibuya, K., Sato, T., Van Dam, T. (1999). Network of superconducting gravimeters benefits a number of disciplines. *EOS, 80, 11, 121/125-126.*

Dehant, V., 1987, Tidal Parameters for an Inelastic Earth. Physics of the Earth and Planetary Interiors, 49, 97-116.

Ducarme B., Timofeev V. Y., Everaerts M., Gornov P. Y., Parovishnii V. A., van Ruymbeke M., 2007, A Trans Siberian tidal gravity

profile (TSP) for the validation of tidal gravity loading corrections. J. of Geodynamics, doi:10.1016/j.jog.2007.07.001.

Ducarme B., Rosat S., Xu J.Q., Vandercoilden L., Sun H.P., 2008, European tidal gravity observations: Comparison with Earth Tides models and estimation of the Free Core Nutation (FCN) parameters. *Accepted for publication* in IAG Proc., Symp. GS003 "Earth Rotation and Geodynamics", XXIV IUGG General Assembly, Perugia, I.

Eanes, R., Bettadpur S., 1996, The CSR3.0 global ocean tide model: Diurnal and Semi-diurnal ocean tides from TOPEX/POSEIDON altimetry, CRS-TM-96-05, Univ. of Texas, Centre for Space Research, Austin, Texas

Fang, J., 1984, The solid Earth tides. Science press, Beijing, P.30-79 (in Chinese)

Farrell, W. E., 1972, Deformation of the Earth by surface loads. Rev Geophys Space Phys, 10: 761-797

Goad, C. C., 1980, Gravimetric tidal loading computed from integrated green's function. J Geophys Res, 85: 2679-2683

Melchior P. 1983, The tides of the planet Earth, 2nd ed. Pergamon Press, Oxford, 641 pp.

Schwiderski, E. W., 1980, On charting global ocean tides. Rev Geophys Space Phys, 18 (1) :243-268

Timmen, L., Wenzel, H. G., 1994, Worldwide synthetic gravity tide parameters available on internet. Bulletin D' Informations, Bureau Gravimetrique International, 75: 32-40

Wenzel, H. G., 1996, The nanogal software: Earth tide data processing package ETERNA 3.3. Bulletin d'Informations Marees Terrestres 124: 9425-9439

Zahran, K.H., G. Jentzsch, G. Seeber. 2005, World-wide synthetic tide parameters for gravity and vertical and horizontal displacements. Journal of Geodesy, 79:293-299

Zschau, J. and R. Wang 1981, Imperfect elasticity in the Earth's mantle. Implications for Earth tides and long period deformations. Proceedings of the 9th International Symposium on Earth Tides, New York 1981, editor J.T. Kuo, Schweizerbartsche Verlagsbuchhandlung, Stuttgart 1981, 605-629.

Precursory signal of the last eruption of Mount Etna detected by continuous gravity observations

Abdelbar El Wahabi, Michel van Ruymbeke & Bernard Ducarme
Royal Observatory of Belgium, Avenue Circulaire 3, B-1180 Brussels, Belgium
(Abdelbar.Elwahabi@oma.be - Bernard.Ducarme@oma.be)

Abstract

Mount Etna volcano is characterized by a fractured edifice so that the seismic activity and the ground deformation are often minimal and even insignificant during the pre-eruption phase. In this case, the microgravity represents a good alternative volcano monitoring technique to detect the mass changes in relation with the movement of fresh magma to shallower levels. In 1992, the LaCoste & Romberg gravimeter LCR8 was installed in Serra La Nave station on the Southern flank of the Etna edifice. As the spring gravimeters are strongly influenced by the Earth tides and the meteorological parameters, it was necessary to remove their effects in order to obtain reliable gravity residuals which could be related to the volcanic activity. Before the beginning of the 1995-2001 eruption, the LCR8 recorded gravity variations of about 350 µgal (1µgal = 10nm.s^{-2}), which are clearly correlated with seismic activity and other precursors of the paroxismal activity. These observations are not incompatible with the moderate 40µgal gravity increase at the Etna summit between the September 1994 and October 1995 discrete gravity measurements, due to the epoch of these campaigns.

Introduction

Most emphasis has been put in recent years on the development of volcano monitoring, based on the integration of different geophysical and geochemical techniques. This multidisciplinary approach is largely improving the monitoring reliability.

The 500.000 year-old Mount Etna is the most active volcano in Europe. Its last eruption, which began in 1995, is considered to be the most important one during the last three centuries. It involved the four craters with lateral fractures long of some 6 km on the NE and SE flanks. This eruption was explosive, characterized by many violent episodes with strong gas emissions, lava fontaining, big ash panaches, etc. It appears that Mount Etna is becoming more and more explosive indicating a change in its behaviour. According to Schiano et al. (2001), the volcanism of Mount Etna is now in a transition phase from a mantle plume source to an island arc source.

It has already been stressed that Mount Etna eruptions occur without significant precursory signals as the seismic activity and the ground deformation remain often minimal (McGuire et al., 1995; Rymer et al., 1993). In these conditions, only the microgravimetry is able to detect the mass changes associated with the emplacement of fresh magma at shallower depth. However, if microgravimetry survey is an usual tool, few examples of continuous gravity observations on volcanoes exist and none lead to any conclusive results.

Taking these facts into account, our gravimetric investigations were oriented in 1992 to the monitoring of the Mount Etna in Sicily, one of the selected European laboratory volcanoes. The LaCoste & Romberg gravimeter LCR8 was installed in Serra La Nave Observatory, situated on the South flank of the volcanic edifice near the SE crater (see figure 1), and continuously recorded gravity variations from 1992 till 1995. As the gravity changes due to volcanic activity are very small compared to other geophysical or instrumental effects, several corrections are needed to get reliable gravity residuals susceptible to reflect the volcanic effect. For this purpose we developed correction algorithms for different perturbing signals like Earth tides, atmospheric pressure and ambient temperature and humidity.

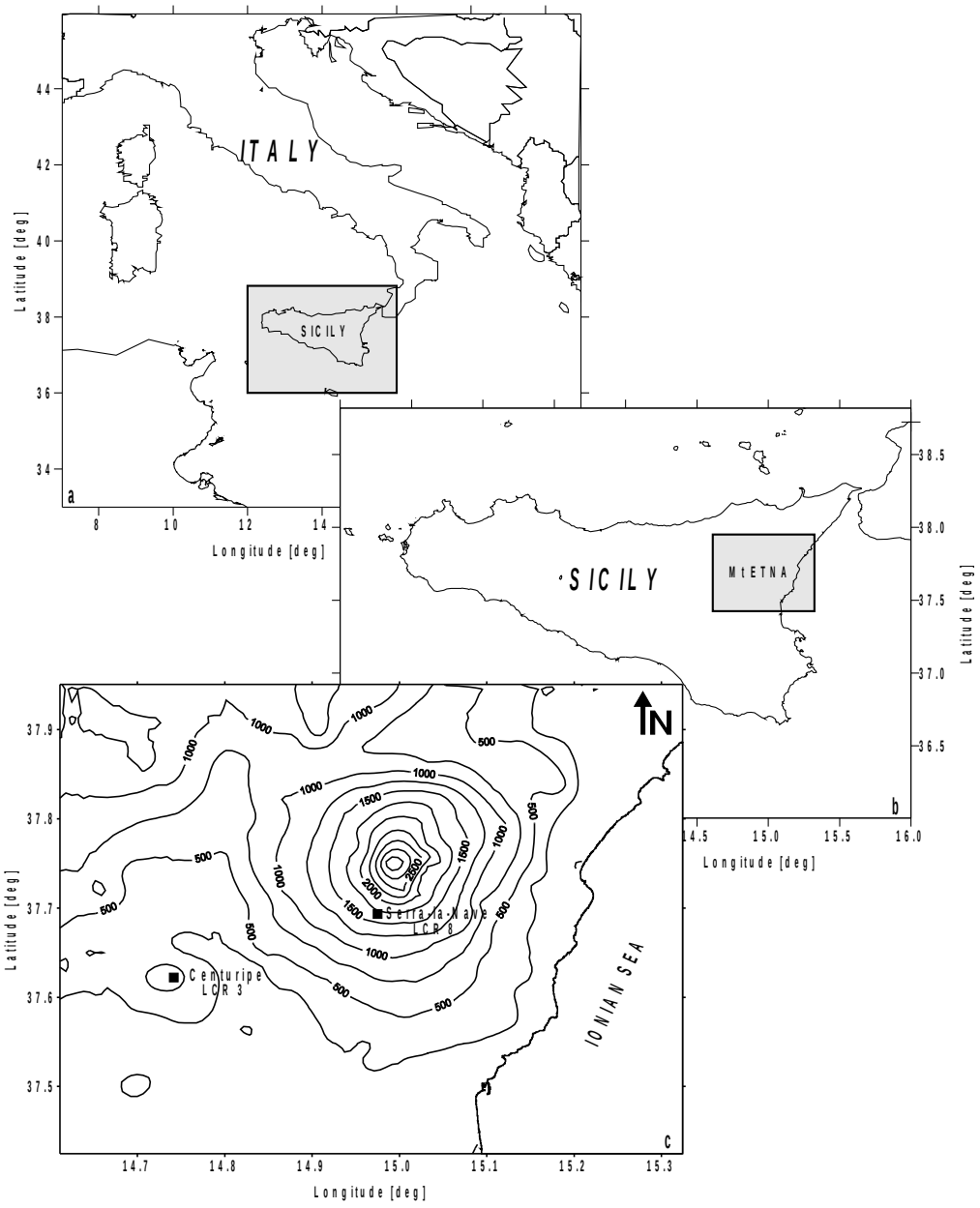

Fig. 1 – (a) = map showing the Sicily localisation in the South of Italy, **(b)** = map showing the Etna volcano position in the NE of Sicily, **(c)** = Topographic map of Mount Etna showing the position of Serra La Nave (SLN) station where the gravimeter LCR8 was installed.

Data processing

We first analyse the Earth tides effect (Eterna, Wenzel 1996) which can be thus modelled with high accuracy and removed efficiently from the raw gravity measurements (TET in figure 2 a and b) (El Wahabi et al., 1997). The residues are often called "drift".

Considering the fact that, for the final residuals, we are looking for a precision of about 1 µgal for a period of one day, a simple linear regression using the local pressure is sufficient to correct the air pressure effect. It was found that we can correct the atmospheric pressure influence on the LCR8 gravity readings by two different regression coefficients close to –1.2 µgal/mbar for the short period and –1.9 µgal/mbar for long period variations (P in figure 2 d, e and f). These coefficients are very high and indicating that this gravimeter is not well compensated any more for air pressure variations and this probably because the pressure seals are not more airtight (El Wahabi et al., 1997).

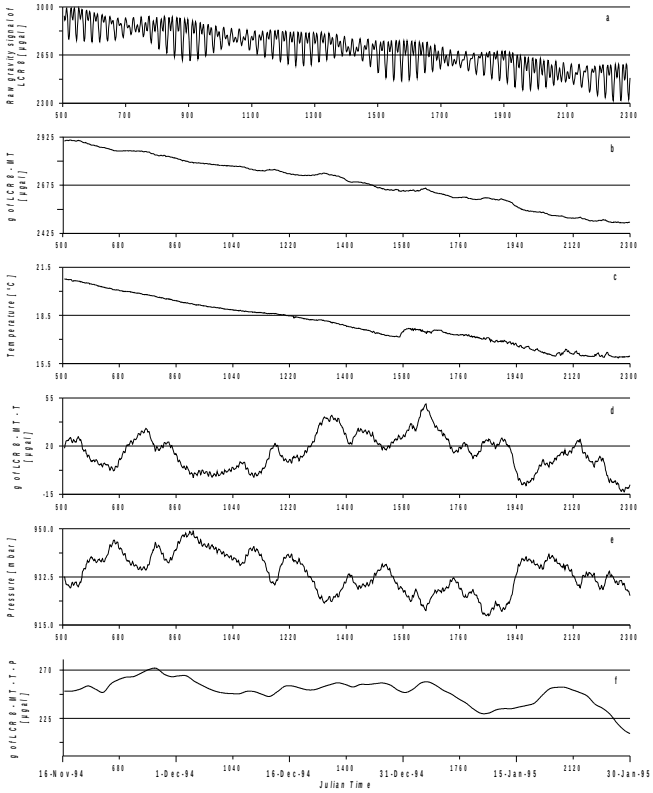

Fig. 2 – Data recorded at Serra La Nave station from 16/11/1994 to 30/01/1995. (a) = raw gravity data of LCR8, (b) = gravity residuals after removing Theoretical Earth Tides (TET), (c) = temperature records, (d) = gravity residuals after removing TET and Temperature Tendancy (TT), (e) = pressure records, (f) = final gravity residuals after removing TET, TT and Pressure effect (P).

Generally, continuous gravity recordings show a large annual variation of the drift as a common feature, with a magnitude ranging from hundreds of microgals to a few mgals. This drift usually presents for the LCR gravimeters an obvious correlation with temperature variations (TT in figure 2 b, c, d and figure 3). It is not astonishing as variations of the ambient temperature affect directly the operation of the thermostat of the gravimeter. However, in some stations (Pecny, Potsdam), where the temperature is controlled with an accuracy of ± 0.1°C, tidal gravimeters still show large annual variations in their drift. As a matter of fact, the experiment of Bastien and Goodacre (1990) has shown that, in a controlled environment, the air humidity may be directly responsible for the gravimeters drift as well. Finally, our experiment in the thermostatized fundamental station of the Royal Observatory of Belgium (ROB) (El Wahabi et al., 2000, 2001) led us to consider that the humidity was the responsible parameter for the annual oscillations present in the LCR8 drift and, more generally, that LCR gravimeters react as humidity integrators. The sensitivity of these instruments to humidity variations is thus inversely proportional to the associated frequency. The annual wave is thus largely dominating the spectrum of the instrumental response to humidity variations.

In Serra la Nave we had temperature measurements but no sensor for humidity. However our experiments at ROB have shown that natural humidity variations in the vault followed external humidity variations, which in turn are anticorrelated with temperature. External temperature represents thus a good proxy of humidity. This fact is confirmed at Serra la Nave where a cross-correlation shows a phase lag of about 70 days of the gravity signal with respect to the temperature variations outside the station (in the open air). Bastien and Goodacre (1990) obtained a similar result in Ottawa between ET-12 gravimeter and outdoor absolute humidity which was leading the gravity residuals drift by some 60 days.

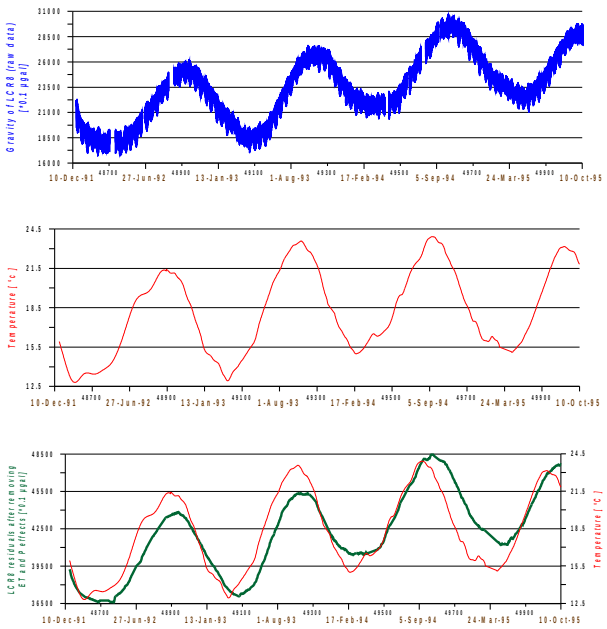

Fig. 3 – Top : raw gravity signal of LCR8 gravimeter recorded in Serra La Nave station for the period 1992-1995 ; middle : temperature variations ; bottom : gravity residuals (Earth tides and pressure effects removed) compared with temperature variations.

To account for the large frequency spectrum of the perturbing temperature and humidity signals, we determined the impulse response of the system (De Meyer, 1982) with respect to external temperature used as a proxy of the perturbing signals. We were thus able to remove the annual wave and its harmonics and obtained the final gravity residuals illustrated in figure 4.

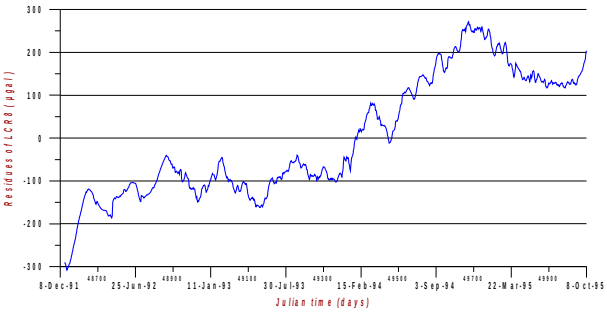

Fig. 4 – Final gravity residuals of LCR8 gravimeter (SLN) for the period 1992-1995.

These final residuals present now the raw material to be correlated with geophysical parameters. Comparing these residuals to the raw data, we notice a significant attenuation of the signal. The Fast Fourier Transfer (FFT) analysis in amplitude shows only red noise (Figure 5),
indicating an efficient correction of the periodic signals. It is therefore clear that the slower the gravity variations the higher the detection threshold. If we consider that an event must be 3 times bigger than the noise level, the one week detection threshold is about 9 µgal for LCR 8.

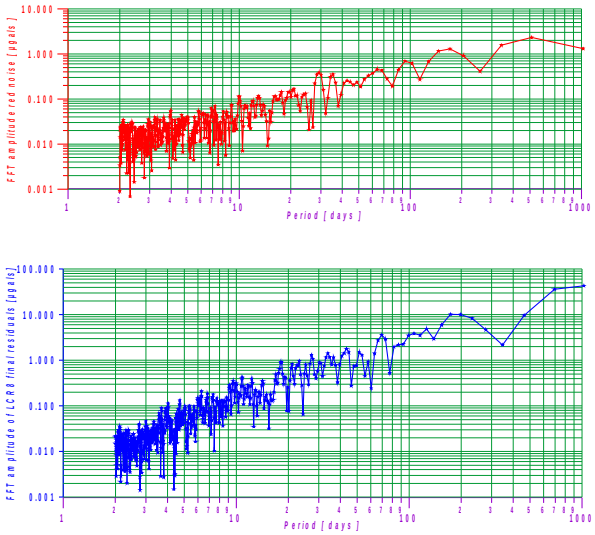

Fig. 5 – Top : FFT analysis for a red noise generated with a standard deviation equal to 1. Bottom : FFT analysis for LCR 8 final gravity residuals.

Correlation between gravity residuals and volcanic activity

Microgravity studies over some 20 volcanoes in the world showed that volcanic activity produce gravity changes of some tens to hundreds of microgals (Rymer, 1996). These gravity variations could be related to the ground deformation (inflation and deflation edifice) and/or the density changes. Basaltic shields and rifts like Krafla (Iceland), Kilauea (Hawaii) and Etna (Sicily) showed large gravity variations (over hundred of microgals) and small elevation changes. The Etna eruption of December 1991 was indeed preceded by negligible ground deformation (Rymer, 1996).

The curve of these residuals show a gravity increase of about 350 µgal, between January 1994 and January 1995, before the first activity observed at the summit craters of Mount Etna materialised by some ash emissions (Armienti et al., 1996) (see figure 7). The beginning of this gravity increase coincides with a slight increase of the seismic activity (La Volpe et al., 1999) (see figure 6). As the GPS technique did not record any inflation between 1993 and 1995 on the southern part of Etna edifice (La Volpe et al, 1999) where the LCR8 gravimeter was installed, the 350 µgal gravity residual changes of LCR8 could be considered as related to the magma rising before the 1995 Etna eruption.

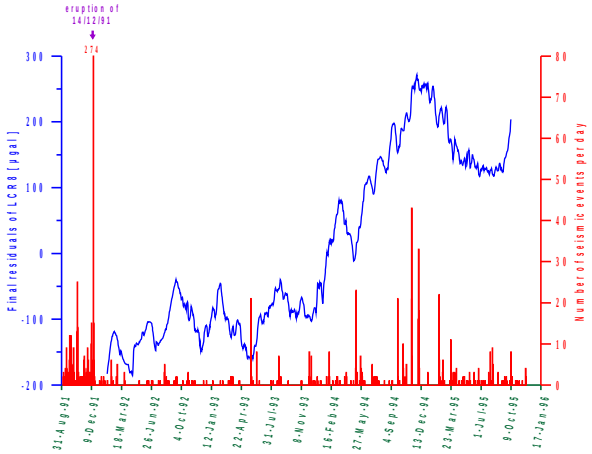

Fig. 6 – Correlation between the final residuals of LCR8 and the daily seismic activity at Serra La Nave station (from “Stato del Vulcan Etna” reports of the International institute of volcanology of Catane).

Once reaching a maximum, the gravity variations started decreasing before changing their trend with a new increase while it was occurring strong Strombolian activity at the summit craters (see figure 7).

We propose a mechanism to explain the beginning of the 1995-2001 eruption of Mount Etna in agreement with our gravity observations. In this mechanism, the magma, moved by virtue of its gravitational buoyancy, rises from its source (probably located at the crust-mantle boundary, at about 27 km depth) and fills a shallow reservoir (Wadge, 1982; Armienti et al., 1984) (plexus of dykes) within or just bellow the volcanic edifice. This first step occurred some months before the beginning of the 1995-2001 eruption and corresponds to the observed increase in gravity. During the second step, corresponding to the period of repose prior the eruption, the temperature and the lithospheric pressure of the magma decrease at this level of depth so that the processes of crystallisation and
vesiculation may start, leading to a vertical segregation of the magma. Therefore, a vertical density gradient would be expected to appear in the reservoir as a result of an upward accumulation of volatiles and other light components to the top and a downward accumulation of heavy components to the bottom. The consequence of these processes is a downward displacement of the centre of mass of the magma corresponding to the decrease of the

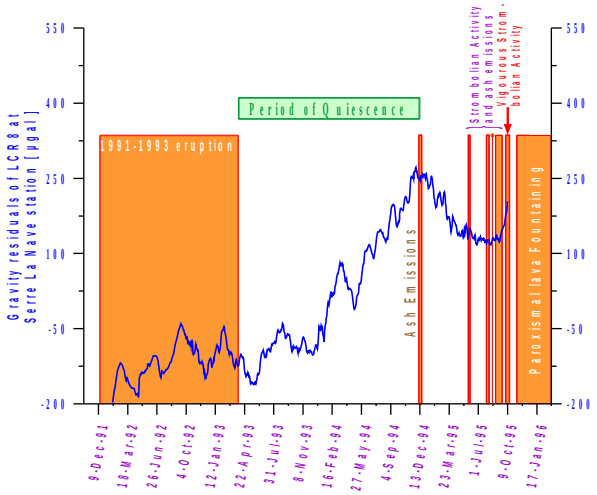

Fig. 7 – Correlation between the gravity residuals of the gravimeter LCR8 and the observed volcanic activity (Armienti et al, 1996) of Mount Etna for the period 1992-1995.

observed gravity. The over-saturation of the magma in volatiles would then trigger the eruption which would lead to the second increase in the gravity variations.

Comparison with discrete gravity measurements

Carbone and Greco (2007) propose an interpretation of discrete gravity measurements at Mt. Etna from 1994 to 1996. They use the quasi NS summit profile, which does not include SLN station. They observe a 40µgal gravity increase around the summit between September 1994 and October 1995 and propose a spherical source beneath the central craters, 2000m below the surface. It is roughly 500m below SLN but quite excentered. It is followed, between October 1995 and July 1996, by a withdrawal of mass from the central zone and the injection of a dyke to the SSE. These observations are not necessarily incompatible with Fig. 7, as the gravity at Serra la Nave had already increased of 200 µgal in September 1994 and the maximum of gravity was already overstepped in October 1995. This campaign corresponds to the final increase of gravity observed in September 1995 at SLN. Our opinion is that the summit observations reported by Carbone and Greco reflect only local gravity changes associated with shallow mass transfer, while continuous gravity changes recorded at SLN recorded deep phenomena with a large spatial extension.

Conclusions

The correction algorithms of all the known perturbations (earth tides, air pressure, temperature and humidity) have been improved to obtain the best final gravity residuals which can be correlated with other geophysical signals of volcanic origin. This correlation leads to the conclusion that continuous microgravity monitoring proves to be an efficient technique for the prevision of volcanic eruptions. So, it is very important to combine the continuous and discrete microgravity observations with the other geophysical and geochemical techniques in order to improve volcanoes monitoring.
Continuous gravity monitoring will only provide significant results after correction of all the geophysical and instrumental perturbing effects i.e. tides, pressure, temperature and humidity. The tidal gravity station at Serra La Nave is well located to detect possible gravity changes associated to the deep volcanic activity of Mount Etna.
The results of simultaneous discrete gravity campaigns depended strongly of their timing as they can only provide snapshots of the mass transfer. Due to the limited extension of the network and the lack of absolute gravity reference they were not able to detect deep mass transfers producing large scale gravity variations.

Acknowledgements

The tidal gravity observations were performed in the framework of the European contract SC-CT91-0700, “Volcanic Deformation and Tidal Gravity Effects at Mount Etna”.
A part of the analysis has been done by Marc Hendrickx and special thanks go to him for his help. The authors are grateful to Nicolas d’Oreye and André Somerhausen who installed the tidal gravimetric station at Serra la Nave. The daily maintenance of the station was insured by Antonio Distefano.

References

Armienti, P., Barberi, F., Innocenti, F., Pompilio, M., Romero, R. & Villari, L. (1984): Compositional variation in the 1983 and other recent Etnean lavas : insights on the shallow feeding system. Bull. Volcanol. 47 (4/2), 995-1007.

Armienti, P., D'Orazio, M., Innocenti, F., Tonarini, S. & Villari, L. (1996): October 1995-February 1996 Mt. Etna explosive activity : Trace element and isotopic constraints on the feeding system. Acta Vulcanologica. 8 (1), 1-6.

Bastien, R. & Goodacre, A.K. (1990): The effect of humidity variations on long-term tidal gravity recordings, Bull. Inf. Marées Terrestres, 106, 7506-7510.

Carbone, D., Greco, F. (2007): Review of microgravity observations at Mt. Etna: a powerful tool to monitor and study active volcanoes, Deformation and Gravity Change: indicators of isostasy, tectonics, volcanism and climate change, PAGEOPH, 164, 4, 769-790.

De Meyer, F. (1982): A Multi Input - Single Output model for Earth tides Data. Bull. Inf. Marées Terrestres. 88, 5628-5674.

El Wahabi, A., Ducarme, B., Van Ruymbeke, M., d'Oreye, N. & Somerhausen, A. (1997): Continuous gravity observations at Mount Etna (Sicily) and correlations between temperature and gravimetric records. Cahiers du Centre Européen de Géodynamique et de Séismologie. 14, 105-120.

El Wahabi, A., Ducarme, B., Van Ruymbeke, M., d'Oreye, N. & Somerhausen, A. (1998): Four years of continuous gravity observations at Mount Etna (Sicily). Proceedings of the 13th International Symposium on Earth Tides, Brussels, Belgium. 477-479.

El Wahabi, A., Dittfeld, H.-J. & Simon, Z. (2000): Meteorological influence on tidal gravimeter drift. Cahiers du Centre Européen de Géodynamique et de Séismologie. 17, 217-228.

El Wahabi, A., Ducarme, B. & Van Ruymbeke, M. (2001): Humidity and temperature effects on LaCoste & Romberg gravimeters. Proceedings of the 14th International Symposium on Earth Tides, Mizusawa, Japan, J. Geodetic Soc. Japan. 47 (1), 10-15.

La Volpe, L., Manetti, P., Trigila, R. & Villari, L. (1999): Volcanology and chemistry of the Earth's interior : Italian research activity (1995-1998) report to IAVCEI. Boll. Geof. Teor. Appli. 40 (2), 163-298.

McGuire, B., Kilburn, Ch.R.J. & Murray, J. (1995): Monitoring active volcanoes : strategies, procedures and techniques. UCL Press Ltd., London, 421 p.

Rymer, H., Murray, J.B., Brown, G.C., Ferruchi, F. & Mcguire, W.J. (1993): Mechanisms of magma eruption and emplacement at Mt Etna between 1989 and 1992. Nature. 361, 439-441.

Rymer, H. (1996): Microgravity monitoring, In Monitoring and mitigation of volcano hazards, Scarpa-Tilling Eds., Springer, p.169-197.

Sanderson, T.J.O. (1982): Direct gravimetric detection of magma movements at Mount Etna. Nature. 297, 487-490.

Schiano, P., Clocchiatti, R., Ottolini, L. & Busà, T. (2001): Transition of Mount Etna lavas from a mantle-plume to an island-arc magmatic source. Nature. 412, 900-904.

Scott, S.C. (1983): Variations in lava composition during the March 1981 eruption of Mount Etna and the implications of a compositional comparison with earlier historic eruptions. Bull. Volcanol. 46, 393-412.

Wadge, G. (1977): The storage and release of magma on Mt Etna. J. Volcanol. Geotherm. Res. 2 (4), 361-384.

Wenzel, H.-G. (1996): The nanogal software : Earth tide data processing package : Eterna 3.3, Bull. Inf. Marées Terrestres, 124, p. 9425-9439.

Localization and estimation of jumps, hidden frequencies and other perturbations in the Earth tide residues

Angel Venedikov[1†)], Bernard Ducarme[2)]
1) Geophysical Institute & Central Laboratory of Geodesy, Sofia.
2) Research Associate NFSR, Royal Observatory of Belgium. ducarme@oma.be

† Prof. Angel Petkov Venedikov unexpectedly passed away on December 1st 2007

1. Introduction.

The paper deals with the non-tidal component $Y(t)$ of some SG data. $Y(t)$ (t is time) is determined as drift of the data through the tidal analysis by the VAV program (Venedikov et al., 2003, 2005). The analysis takes into account all tidal constituents, including the LP tides. Thus $Y(t)$ is expected to be free of all tidal signals.

The aim of the investigation is finding non-tidal signals. They can be useful, e.g. as potential or eventual earthquake and volcano precursors, as well as non-useful or parasite components of the data, which should be removed from the data.

The investigation discussed here is an application of our new program for regression analysis called M-LEVEL. It can deal with the following signals:

(i) Sudden jumps or very fast displacement of the curve $Y(t)$ and sudden or very fast changes in the slope of the curve $Y(t)$, i.e. in the derivatives of $Y(t)$.

(ii) Intervals of $Y(t)$ with anomalies or perturbations and

(iii) Non-tidal waves with known and unknown frequencies.

These items have been successfully applied in (Ducarme et al., 2006a, b). Here a series of superconducting gravity (SG) data is studied in a somewhat more advanced way.

2. General model of the non-tidal data $Y(t)$.

The VAV analysis is made by using filters of 24^h, moved also by 24^h. Each application of the filters provides one value of $Y(t)$. Due to this the unit of the time t used is 1 day. Thus the set of data generally looks like

$$Y(t), t = t_1, t_2, \ldots t_N, \text{ where } t_{i+1} - t_i \begin{cases} = 1 \text{ day when there is not a gap} \\ > 1 \text{ day when there is a gap} \end{cases} \quad (1)$$

In principles, the gaps are not an obstacle, because the processing is made by the Least Square Method (LSM) which allows avoiding artificial creation of data through interpolation. We shall recall the simple principle of dealing with gaps by LSM: LSM deals with the really existing data and it does not deal with data, which do not exist or artificially created.

As shown by Figure 1, the tidal component dominates considerably the non-tidal $Y(t)$, i.e. it should be very carefully eliminated. We hope that this is well done by the tidal analysis program VAV

$Y(t)$ can be conceived as a kind of a mean level of the data, in a way like the mean sea level. Here it looks as a a smooth curve, nearly a constant.

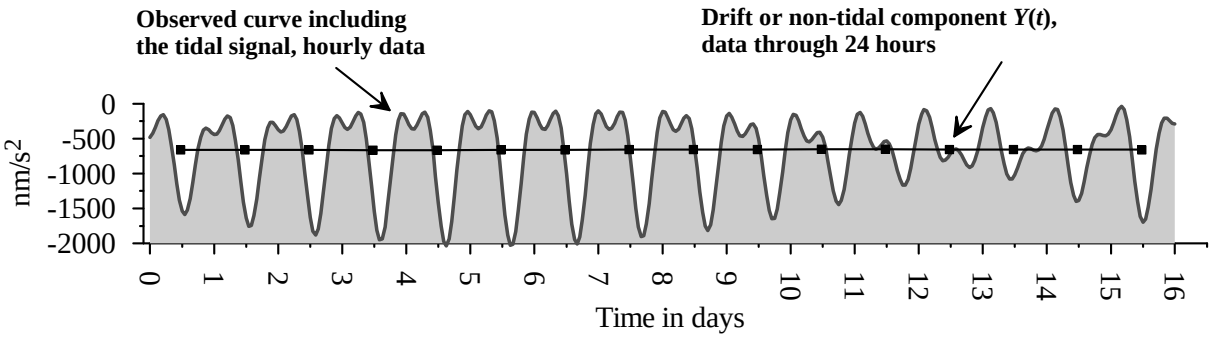

Figure 1. Sample of observed super conducting gravity (SG) tidal data with the non-tidal component $Y(t)$ (black points through 24 hours), station Moxa.

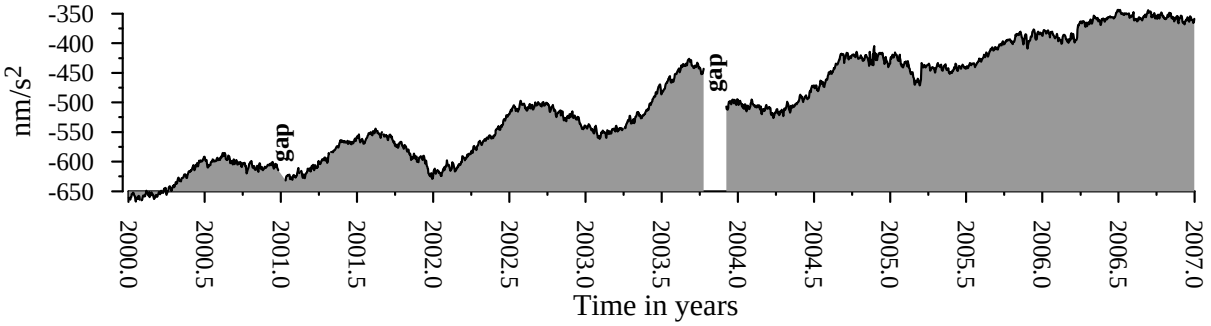

Figure 2. Sample of the non-tidal component $Y(t)$ in another scale, SG station Moxa.

Figure 2 shows, unlike the Figure 1, that actually $Y(t)$ represents a strongly variable phenomenon. Visually, it can be revealed an annual wave plus a proper drift, raising steadily the curve, as well as high frequency oscillations which can be considered as a noise.

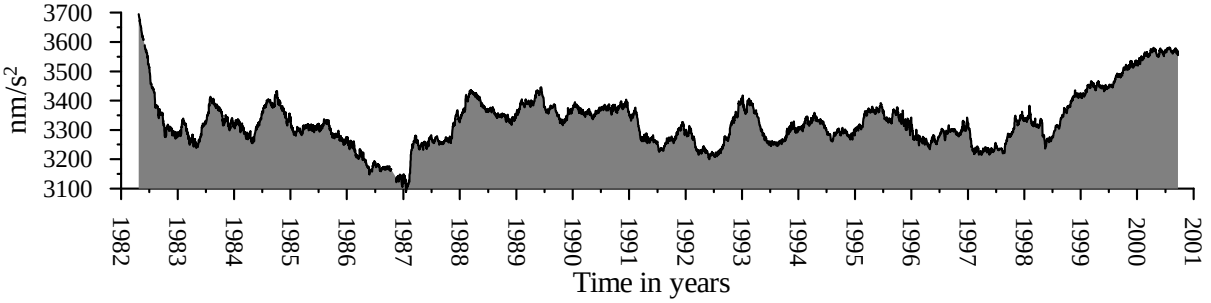

Figure 3. Complete series of the largest and oldest series of the non-tidal $Y(t)$ data from the SG station Brussels.

Figure 3 shows a more sophisticated and intricate series of $Y(t)$ data. It is possible visually to distinguish an annual component, but not such a clear drift with nearly constant slope as in Figure 2.

The task is to find a regression model, well approximating $Y(t)$, i.e. the mean level which includes various non-tidal components or signals

The initial model used here is

$$Y(t) = \sum_{j=1}^{\mu} h_j \cos\left(\varphi_j + \omega_j t\right) + \sum_{k=0}^{K} a_k (t - t_C)^k + \varepsilon_t \qquad (2)$$

where t_C is a central point of the data.

The following parts 2.1 & 2.2 discuss the first two terms of this model. Part 2.3 will discuss some statistical criteria, which are used to estimate some of We shall return to the last term, the noise ε_t, in part XXX.

2.1. Periodic components.

The first term in (1) represents the periodic signals or, may be more precisely, it approximates quasi-periodic signals. The amplitudes h_j and the phases φ_j are unknowns, estimated by the program M-LEVEL, with an application of LSM. Generally, the frequencies ω_j may be also unknowns. Nevertheless, in some of the examples M-LEVEL uses a priori defined values of ω_j, in order to simplify the presentation. Namely the frequencies ω_j expressed in cpy (cycles/year) and the periods in days applied here are given in Table 1.

Table 1. A priory fixed periodic components of the data, used in some of the following examples

ω_1 = 1 cpy, period = 1 year of 365.25 days: annual wave,
ω_2 = 2 cpy, period = 1/2 year: semiannual wave,
ω_3 = 3 cpy, period = 1/3 year: third-annual wave and
ω_4 = 0.842061 cpy, period = 433.76 days: Chandler wave.

In the last parts of the paper (section 5), ω_j are considered as unknown parameters, estimated by a specially developed technology.

Remark about the unit of the frequencies ω_j: In all discussions and results about ω_j the unit used is cpy. However, formally, in expressions like 2, the unit of ω_j should be radians/unit of time. We shall use one and the same denotation ω_j, no matter what is formally the unit used.

2.2. Polynomial component.

This is represented by the second term of (2). In the case of ocean tidal data, this term may be considered as approximation of a variable mean sea level, free of periodic signals. In the case of gravity data, this term can be considered as an approximation of a drift, also free of periodic signals.

Actually, (2) includes the most simple variant of a polynomial approximation. Theoretically, such an approximation is legal when and only when the approximated function of the time is continuous with continuous derivatives.

If Figure 3 is carefully studied, it can be stated that at the start, as well as nearly year 1987 there is a rather fast displacement of the curve, which may be considered as a jump or a

discontinuity of the approximated function. At about July 1999 there is a rather fast change of the general slope of the curve, which has to be considered as a discontinuity of the derivatives. It is of course possible that there are more points of discontinuities which cannot be visually distinguished. Here and further we shall call such a point as D-point.

In the case of 3 D-points, say T_1, T_2 & T_3 they partition the data interval in 4 segments, say S_1, S_2 S_3 & S_4. Then the discontinuity problem is solved by using the model (2) with different polynomials in the different S_i, as shown by the expressions (3).

$$
\begin{aligned}
Y(t) &= \sum_{j=1}^{\mu} h_j \cos(\varphi_j + \omega_j t) + \sum_{k=0}^{K} a_{k1}(t - t_C)^k + \varepsilon_t \quad \text{for } t \in S_1, \text{ i.e. before } T_1 \\
Y(t) &= \sum_{j=1}^{\mu} h_j \cos(\varphi_j + \omega_j t) + \sum_{k=0}^{K} a_{k2}(t - t_C)^k + \varepsilon_t \quad \text{for } t \in S_2, \text{ i.e. between } T_1 \text{ and } T_2 \\
Y(t) &= \sum_{j=1}^{\mu} h_j \cos(\varphi_j + \omega_j t) + \sum_{k=0}^{K} a_{k3}(t - t_C)^k + \varepsilon_t \quad \text{for } t \in S_3, \text{ i.e. between } T_2 \text{ and } T_3 \\
Y(t) &= \sum_{j=1}^{\mu} h_j \cos(\varphi_j + \omega_j t) + \sum_{k=0}^{K} a_{k4}(t - t_C)^k + \varepsilon_t \quad \text{for } t \in S_4, \text{ i.e. after } T_3
\end{aligned}
\tag{3}
$$

Here are 4 sets of different unknown polynomial coefficients a_{ki}, $(i = 1,2,3,4)$, while the unknowns in the periodic terms remain one and the same.

It is obvious, how this scheme can be used for an arbitrary number of D-points and segments.

2.3. Statistical criteria.

When the D-points and the frequencies are known, the estimation of the remaining unknowns, a_{ki}, h_j & φ_j by the LS is a trivial problem. When the D-points and the frequencies are considered as unknowns, the problem is much more sophisticated, because these unknowns take part in a non-linear way.

Our solution of the problem is based on using variations of this kind of unknowns until finding optimum value of a given statistical criterion. D-points

For finding the D-points and the frequencies the Akaike information criterion (Sakamoto et al., 1986) is used, namely

$$\mathrm{AIC} = N(\log \pi + \log \sigma^2 + 1) + 2(N_x + 1) \tag{4}$$

where N is number of the data, N_x is the number of all unknowns and σ^2 is the estimated variance of the data. The optimum value of AIC is its minimum for various models of the data.

In the case, not yet consider, of finding anomalies or perturbations of the data, AIC is not suitable. In this case we use as a criterion the MS error of one of the unknowns, mainly the MS error of the amplitude of the annual component.

3. Finding D-points.

The subscripts of the D-points $T_1,...T_4$ are arranged depending on the depth of the minimum, T_1 being the deepest one.

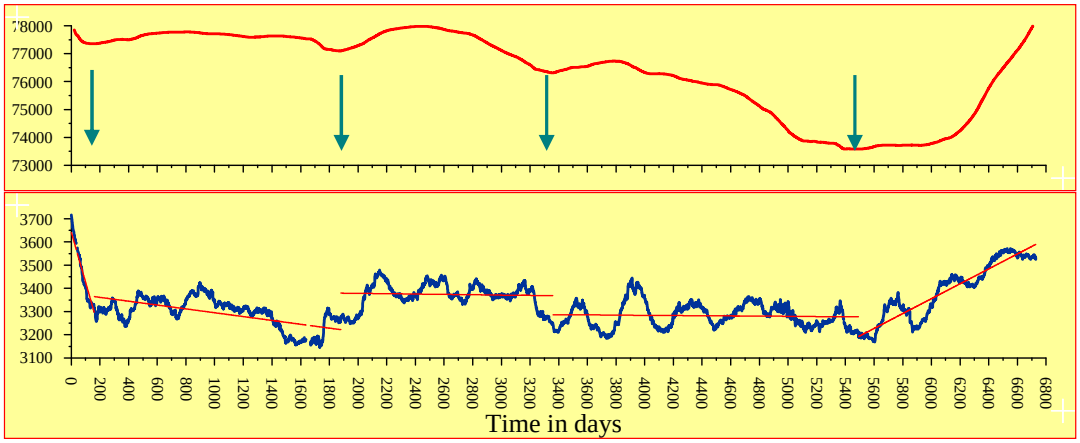

Figure 4. upper: Detection of the minima of the AIC value (arrows) for the data set Brussels, 21.04.1982 - 21.09.20000,

lower: Polynomials $P_1(T)$ (red lines) with 4 D-points AIC=67,574; σ_h = 0.660 nm/s^2

The D-points T_i determined in this way, after an initial creation of pictures like Figure 4, are only initial values. If we need a higher precision, the D-points have to be defined more accurately in an iteration procedure. For the case of 3 D-points this can be done following the following simple algorithm.

1. Fixed T_1 & T_2 $\rightarrow$ let vary T_3 till finding new minimum of AIC.
2. Fixed T_1 & the new T_3 $\rightarrow$ let vary T_2 till finding new minimum of AIC.
3. Fixed the new T_2 & T_3 $\rightarrow$ let vary T_1 till finding new minimum of AIC.
4. Looking for new minima of AIC in the segments defined by the final T_1, T_2 & T_3.
5. If necessary, the procedure can be re-started from item 1.

We find four discontinuities and the adjustment in 5 blocks with polynomials of degree one provides an important improvement with a decrease of both statistical criteria: AIC=67,574; σ_h = 0.660 nm/s^2.

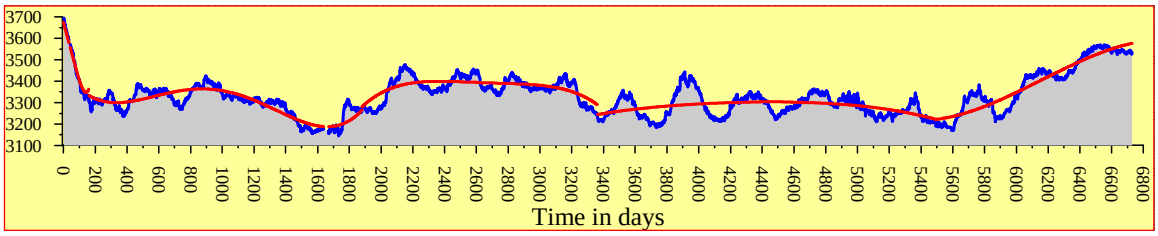

Figure 5. Drift adjustment using a fourth degree polynomial on each block.
Power K = 4: AIC = 62,620, σ_h = 0.471 nm/s^2

Is it possible to get a further improvement by adjusting the degree K of the polynomials? An optimal solution is found with the degree 4 (AIC = 62,620, σ_h = 0.471 nm/s^2, Figure 5).

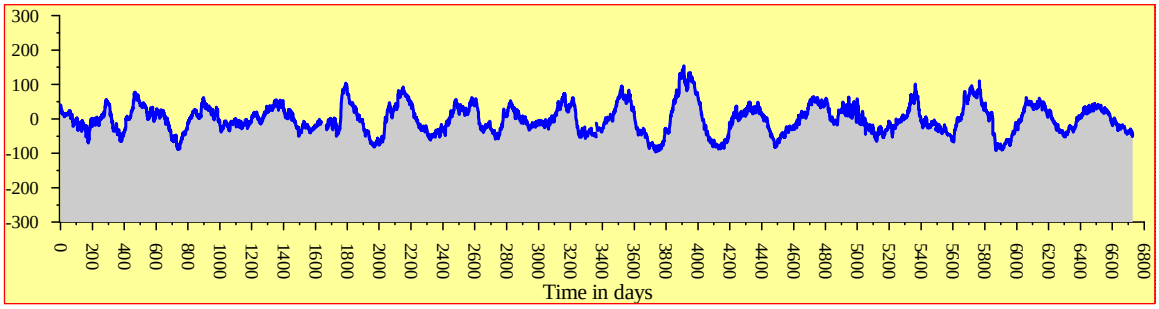

Figure 6. Final representation of the harmonic part of the signal after subtraction of the drift representation in Figure 3.

The harmonic part of the signal is obtained by subtracting the drift representation from the Y(T) series (Figure 6). It is dominated by the annual component and the pole tide signal (section 5 and Ducarme et al., 2005)

4. Detection of anomalous data

Detecting the anomalies in the tidal data is interesting for two reasons:

(i) eliminate them in order to improve the precision and

(ii) using them as particular non-tidal signals, eventually as precursors.

The AIC criterion is only applicable if the data set remains unchanged. For the anomalous data detection and rejection we can only rely on the MSD reduction. In the examples hereafter the statistical criterion used is: σ_h (MSD of the amplitude of the annual wave with frequency 1 cpy) minimum.

Let V1 & V2 be two variants of the processing or/and of the data used.

If $\sigma_h(V2) < \sigma_h(V1)$, the variant V2 should be preferred by the simple reason that V2 provides a higher precision.

In this sense σ_h is used in the same way as the criterion AIC of Akaike above. Actually, there are seldom seen contradictions between these two criteria. Nevertheless, in the case of different eliminations of data, AIC cannot be used, because it should be applied on one and the same sets of data.

Let:

$\sigma_h(0)$ be the value of σ_h when all data in a series are processed,

(t_a, t_b) be a time interval of the data with a central point $t_{ab} = (t_a + t_b)/2$ and

$\sigma_h(t_{ab})$ be the value of σ_h when the processing eliminates the interval (t_a,t_b).

In this sense (t_a, t_b) will be called E-interval (elimination interval).

It should be expected $\sigma_h(0) < \sigma_h(t_{ab})$ because the elimination of the E-interval decreases the quantity of the data and thus decreases the analysis precision.

Hence, if on the contrary $\sigma_h(t_{ab}) < \sigma_h(0)$, this is a serious indication that the E-interval (t_a, t_b) contains some anomalous data or it is a part of an anomaly.

The idea used is the following. We deal with an E-interval (t_a, t_b) with variable limits t_a and t_b. Initially, the E-interval covers m = (b – a + 1) = 11 days. We let run the limits t_a and t_b by increasing both t_a and t_b by steps of 1 day. This is made so that the moving (t_a, t_b) runs along the whole set of the data.
For every position of (t_a,t_b) the program applies the analysis, the data in the interval (t_a, t_b) being excluded (eliminated). In such a way we get our criterion
$\sigma_h = \sigma_h(t_{ab})$ as function of the central point $t_{ab} = (t_a + t_b)/2$
If at t_{ab} in which $\sigma_h(t_{ab})$ has relative minimums, the corresponding interval is almost certainly anomalous and it should be eliminated.
Let us consider the Membach data set 04.08.1995 – 03.12.2006 (Figure 7). The curve of $\sigma_h(t_{ab})$ as function of $t_{ab} = (t_a + t_b)/2$ (central point of the E-interval), displayed in Figure 8, shows 5 relative minimums A1, … A5, clearly indicating anomalous data, e.g. the strongest minimum A1 shows a strong anomaly at the beginning, which is usual.

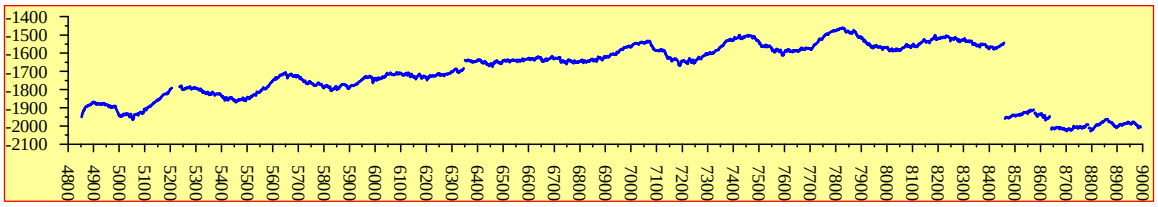

Figure 7. Membach data set 04.08.1995 – 03.12.2006

If we give a closer look to the E-interval A4, we see a rather complex minimum close to the E-interval ($t_a = 7185^d$, $t_b = 7195^d$) in Figure 9.

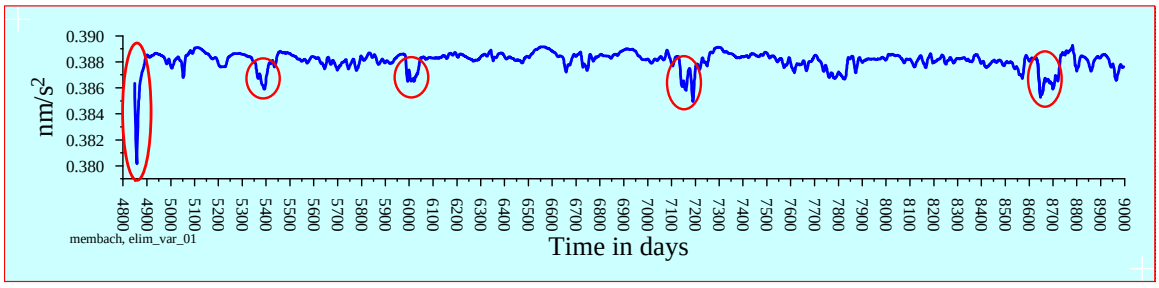

Figure 8. Curve of $\sigma_h(t_{ab})$ as function of $t_{ab} = (t_a + t_b)/2$ (central point of the E-interval) with 5 relative minimums A1, … A5, clearly indicating anomalous data.

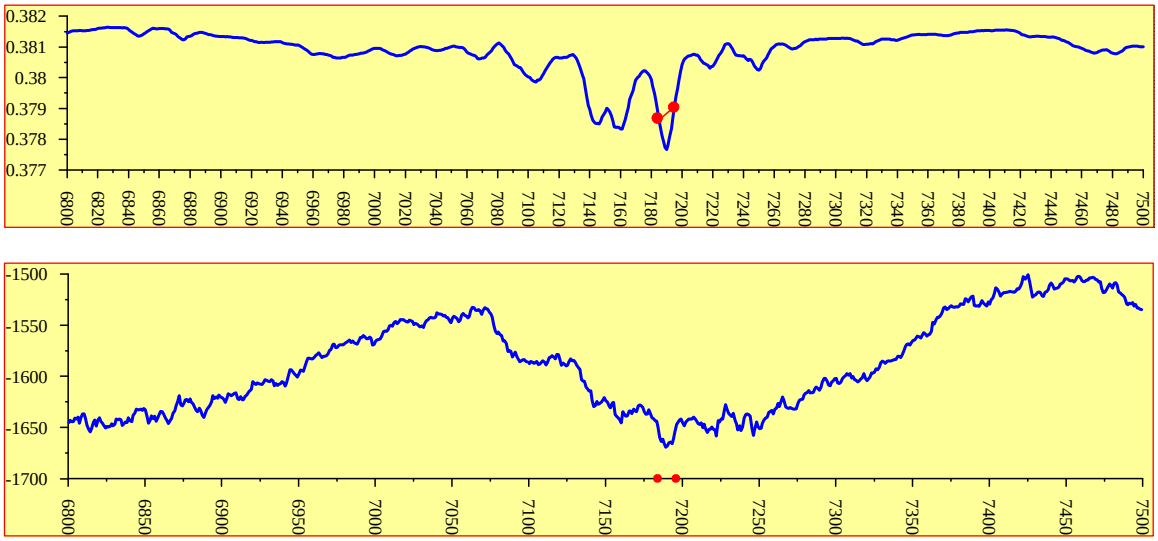

Figure 9. Details around the A4 minimum.

Upper curve: variations of $\sigma_h(t_{ab})$ as function of $t_{ab} = (t_a + t_b)/2$

Lower curve: Y(T) series

Red dots indicate the position of the 10 days interval corresponding to the lowest minimum.

After an initial E-interval is determined, as shown here, JUMP_07 allows variations of the limits t_a & t_b, in opposite directions, in order to find eventually further reduction of the criterion σ_h and thus a modulation of the E-interval for a better precision.

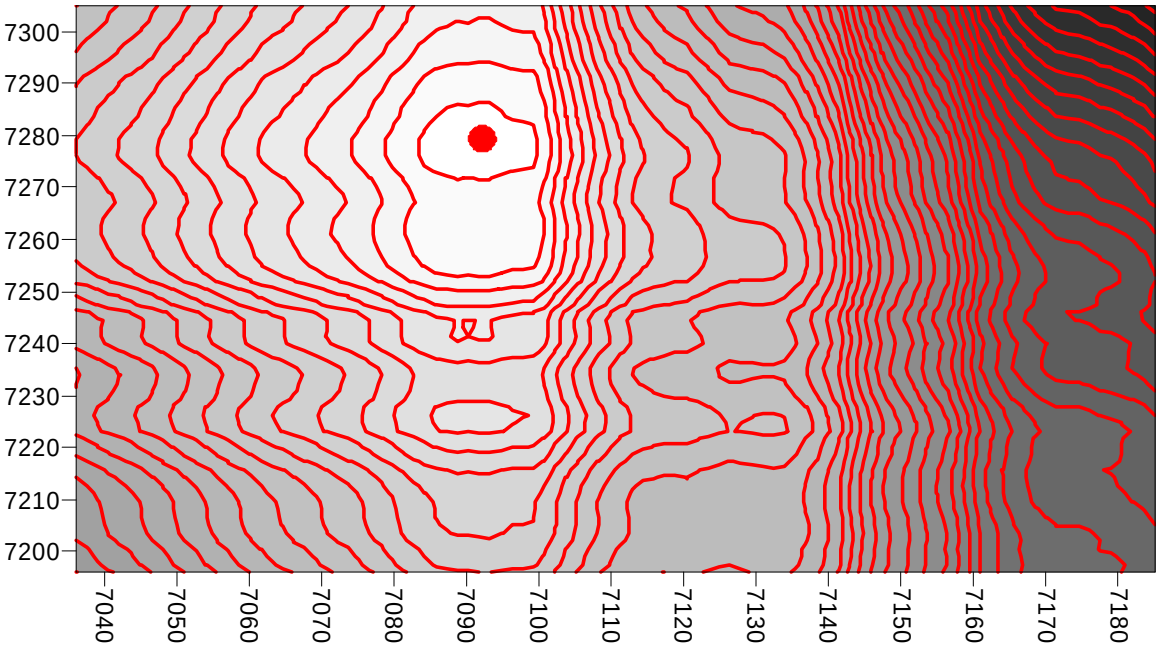

Figure 10. Minimum of $\sigma_h(t_a, t_b)$ at $t_a = 7092^d$ & $t_b = 7276^d$; this means that the E-interval (7092^d, 7276^d) may be eliminated in order to improve the precision.

The variations can be imposed independently on the limits t_a & t_b or symmetrically on both limits. Through the mutual variation we get σ_h in a 3-D space, i.e. $\sigma_h = \sigma_h(t_a, t_b)$ as a function of the two variables t_a and t_b (Figure 10).
A clear minimum is obtained for t_a equal day 7092and t_b equal day 7276. The E-interval (7092^d, 7276^d) may be eliminated in order to improve the precision, although this is a rather large (185 days) interval. Finally the 5 intervals shown in red in Figure 11 were eliminated.
The reduction of the MSD is important, from σ_h = 0.380 nm/s^2 (all data, without eliminations) to σ_h = 0.317 nm/s^2. Such a raise of the precision could be obtained only if the length of the data is increased in the ratio $(0.380/0.317)^2$, i.e. 44%.

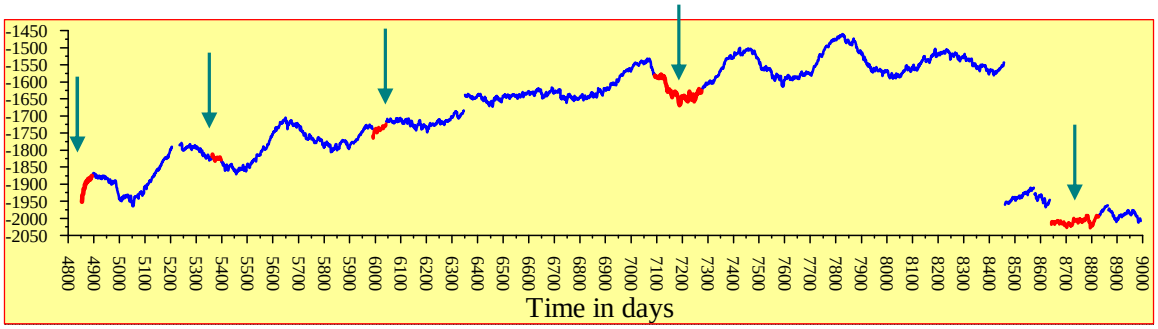

Figure 11. The five eliminated intervals are shown in red

5. Search for non-tidal waves with unknown frequencies

Here also we apply an automatic search algorithm constrained by the AIC criterion.
Instead of looking for the maximum of the amplitude $h = h(\omega)$ as a function of ω, as it is done in the spectral analysis, we shall consider the criterion AIC = AIC(ω) as a function of ω, looking for its minimum. So to say, instead of the spectrum h(ω) we shall deal with the AIC (ω) spectrum.
Let us suppose that we know *m* frequencies ω, i.e. we can solve by LSM the system

$$Y(T) = \sum a_k T^k + \sum (\alpha_j \cos \omega_j T + \beta_j \sin \omega_j T), T = T_1, \ldots T_n \qquad (0.1)$$

Let us call the corresponding value of the Akaike Information Criterion AIC_m.
In a next step we add a new wave with variable ω

$$Y(T) = \sum a_k T^k + \sum (\alpha_j \cos \omega_j T + \beta_j \sin \omega_j T) + \alpha \cos \omega T + \beta \sin \omega T \qquad (0.2)$$

Let us vary the value of ω by steps Δω and for every value of ω we get $AIC_{m+1}(\omega)$.
When we get for a given value $\omega=\omega_{Min}$:

$$AIC_{m+1}(\omega_{Min}) = \text{Minimum}$$

and

$$AIC_{m+1}(\omega_{Min}) < AIC_m,$$

we accept ω_{Min} as a new frequency ω_{m+1} and the procedure can be repeated iteratively

.

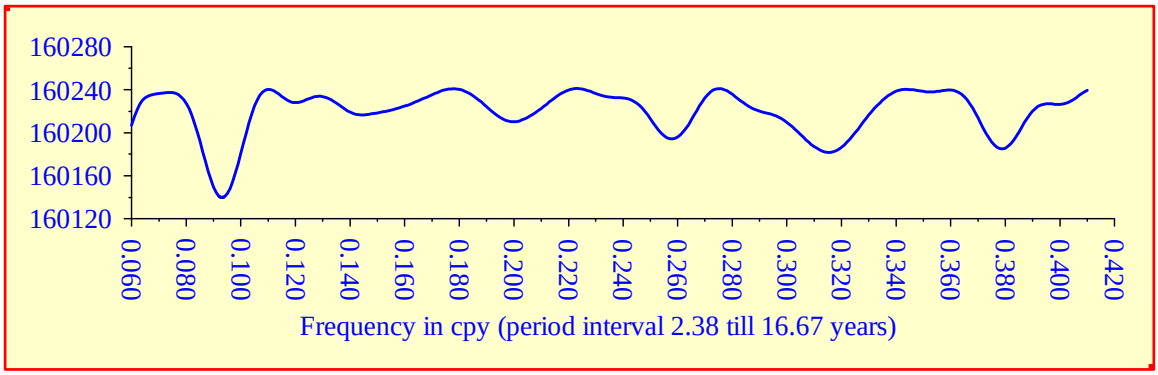

Figure 12. Station Cananéia (Brazil): variation of AIC as a function of a moving frequency showing a minimum at 0.093124 cpy, period = 10.74 years

As an example let us consider first the research of a very low frequency non-tidal component in a 50 year tide gauge record at Cananéia (Brazil) (Ducarme et al., 2006b). An additional harmonic constituent was search between 0.06cpy (16.67y) and 0.42cpy (2.38y). Several relative minima were found, with an absolute one at 0.093124 cpy (period = 10.74 years), corresponding to the solar cycle (Figure 12).
When the existence of two close frequencies is suspected, a simultaneous search is possible that can be represented in a three dimensional space. The example given below illustrates the simultaneous fit of the annual period and the Chandler one on the Brussels data of Figure 6. An absolute AIC minimum is found in Figure 13 at a point corresponding to periods (365.12, 433.76 days) or frequencies (1.00037, 0.842061 cpy).

6. Conclusions

A program M-LEVEL has been developed to exploit fully the possibilities of the VAV tidal analysis program. Starting from the daily values Y(T) of the residues obtained automatically from VAV by subtracting the full tidal signal, it allows to detect anomalies and jumps in the data as well as unknown non-tidal frequencies. The procedure is based on the use of statistical criteria to find the optimal regression model or the best part of a data set. The Akaike Information Criterion (AIC) is used in parallel with the Mean square Deviation (MSD) of the adjusted parameters. The best solution coincides with the lowest value of these statistical quantities. The procedure is very flexible.

Bibliography

Ducarme B., van Ruymbeke M., Venedikov A.P., Arnoso J., Vieira R., 2005.
Polar motion and non tidal signals in the superconducting gravimeter observations in Brussels.
Bull. Inf. Marées Terrestres, 140, 11153-11171.
Ducarme B., Venedikov A.P., Arnoso J., Chen X.D., Sun H.P., Vieira R., 2006a.
Global analysis of the GGP superconducting gravimeters network for the estimation of the pole tide gravimetric amplitude factor. *Proc. 15th Int. Symp. On Earth Tides, J. of Geodynamics, 41, 334-344.*
Ducarme B., Venedikov A.P., de Mesquita A.R., De Sampaio França C.A., Costa D.S., Blitzkow D., Vieira R., Freitas S.R.C., 2006b. New analysis of a 50 years tide gauge record at Cananéia (SP-Brazil) with the VAV tidal analysis program. *Dynamic Planet, Cairns, Australia, 22-26 August, 2005. Springer, IAG Symposia, 130, 453-460.*

Sakamoto Y., Ishiguro M., Kitagawa G. 1986. Akaike information criterion statistics, *D. Reidel Publishing Company, Tokyo*, 290 pp.
Venedikov, A. P., Arnoso, J., Vieira, R. (2003). VAV: a program for tidal data processing. *Comput. Geosci., 29, 487-502.*
Venedikov, A. P., Arnoso, J., Vieira, R. (2005). New version of the program VAV for tidal data processing. *Comput. Geosci., 31, 667-669*

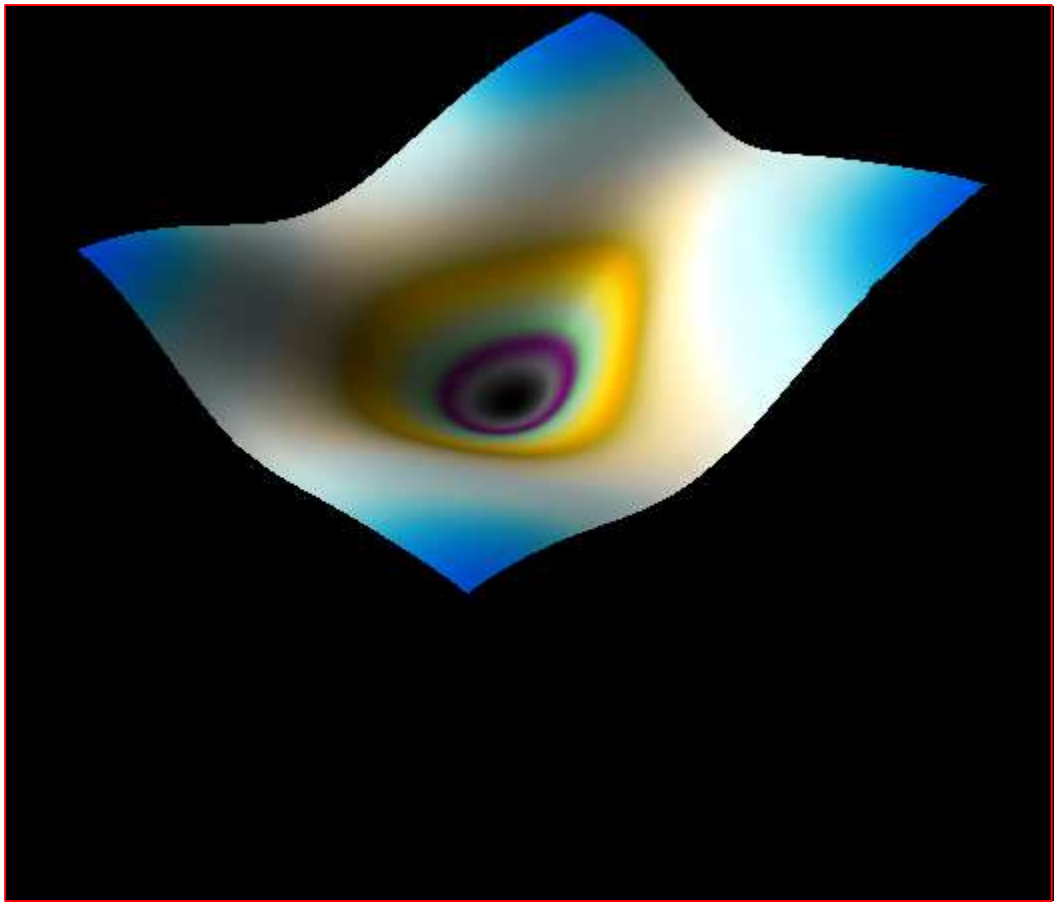

Figure 13. Three dimension graph showing the existence of two close frequencies in the Brussels data, an annual one at 1.00037cpy (365.12 days) and the Chandler one at 0.842061cpy (433.76 days)

IN MEMORIAM

Prof. Dr. Angel Petkov Venedikov
Geophysical Institute and Central Laboratory on Geodesy,
Bulgarian Academy of Sciences

Angel Venedikov was born in Sofia on July 5 1936.
He got his university degree in Geodesy and was working since 1960 in the Geophysical Institute of the Bulgarian Academy of Sciences. After a specialization on the Earth Tides in 1963 at the Geophysical Institute in Prague, he made a pioneer work in the field of the tidal analysis methods. As early as 1966 he developed at the Royal Observatory of Belgium (ROB), in cooperation with Paul Melchior and Paul Pâquet, a new method and computer program for analysis of the Earth tides, which allowed for the first time the processing of data with gaps of arbitrary length, with a correct application of the Method of the Least Squares. This program VEN66 was used as a standard analysis method by ROB and the International Center for Earth Tides (ICET) during thirty years. It is only recently that this program has been definitely replaced by more performing methods such as new versions of his method, the VAV programs developed at the "Instituto de Astronomía y Geodesia (CSIC-UCM)" in Madrid, in collaboration with Ricardo Vieira and his group, or the ETERNA and BAYTAP-G software. He has been very active until his last moment and was still developing new applications of the VAV method to ocean tides analysis.

Another important orientation of his work was the study of anomalies in the records i.e. non-tidal signals, some of which can appear to be earthquake and volcano precursors. This work started in 1985 in Spain for the monitoring of the volcanic activity in the Canary Islands. It was developed also in Kiel, Germany (1989, German-Turkish Seismological Project), China (1987), Japan (1991), Potsdam (1996)….

In 1975 he organized the International Computing Laboratory for Earth Tides, which used to collect and process all tidal data of the Countries of Eastern Europe till 1989.
He assumed different responsibilities in the Geophysical Institute and in the Academy of Sciences.

Angel Venedikov was corresponding member of the Bulgarian Academy of Sciences and foreign corresponding member (Académico Correspondiente Extranjero) of the Royal Academy of Sciences of Spain (Ciencias Exactas, Físicas y Naturales). It has been invited Professor at the Universities of Uppsala (1973), Kiel (1989) and Vigo (1999). He has been visiting scientist in many Institutes or Universities, where he developed his personal research. Between 1965 and 2007 he was visiting nearly 20 times the International Centre for Earth Tides (ICET) at the Royal Observatory of Belgium in Brussels.

Angel Venedikov is author or co-author of some 130 publications, which have been cited more than 4,000 times in some 850 foreign publications.

Angel passed away on December 1st. 2007 as result of heart attack.

Bernard Ducarme
ICET Director